Title
ILC3s control splenic cDC homeostasis via lymphotoxin signaling

Journal
Journal of Experimental Medicine, 218(5)

ISSN
0022-1007

Authors
Vanderkerken, Matthias
Baptista, Antonio P
De Giovanni, Marco
et al.

Publication Date
2021-05-03

DOI
10.1084/jem.20190835

Peer reviewed

JEM Journal of Experimental Medicine

BRIEF DEFINITIVE REPORT

ILC3s control splenic cDC homeostasis via lymphotoxin signaling

Matthias Vanderkerken[1,2*], Antonio P. Baptista[1,2*], Marco De Giovanni[3*], Satoshi Fukuyama[4], Robin Browaeys[5,6], Charlotte L. Scott[7,8], Paula S. Norris[9], Gerard Eberl[10,11], James P. Di Santo[12,13], Eric Vivier[14,15,16], Yvan Saeys[5,6], Hamida Hammad[1,2], Jason G. Cyster[3], Carl F. Ware[9], Alexei V. Tumanov[17**], Carl De Trez[18**], and Bart N. Lambrecht[1,2,19**]

The spleen contains a myriad of conventional dendritic cell (cDC) subsets that protect against systemic pathogen dissemination by bridging antigen detection to the induction of adaptive immunity. How cDC subsets differentiate in the splenic environment is poorly understood. Here, we report that $LT\alpha_1\beta_2$-expressing Rorgt$^+$ ILC3s, together with B cells, control the splenic cDC niche size and the terminal differentiation of Sirpα$^+$CD4$^+$Esam$^+$ cDC2s, independently of the microbiota and of bone marrow pre-cDC output. Whereas the size of the splenic cDC niche depended on lymphotoxin signaling only during a restricted time frame, the homeostasis of Sirpα$^+$CD4$^+$Esam$^+$ cDC2s required continuous lymphotoxin input. This latter property made Sirpα$^+$CD4$^+$Esam$^+$ cDC2s uniquely susceptible to pharmacological interventions with LTβR agonists and antagonists and to ILC reconstitution strategies. Together, our findings demonstrate that $LT\alpha_1\beta_2$-expressing Rorgt$^+$ ILC3s drive splenic cDC differentiation and highlight the critical role of ILC3s as perpetual regulators of lymphoid tissue homeostasis.

Introduction

Host protection requires continuous detection and response to an overwhelming myriad of pathogenic insults. By their widespread tissue distribution and unrivaled capacity to recognize danger-associated signals and process and present pathogen-derived antigens, conventional dendritic cells (cDCs) are essential components against disease. Tissue cDCs derive from bone marrow pre-cDC progenitors that circulate in the bloodstream and continuously seed tissues (Liu et al., 2009; Naik et al., 2007). Whereas pre-cDC commitment to cDC1 or cDC2 fate seems to begin in the bone marrow (Grajales-Reyes et al., 2015; Schlitzer et al., 2015), terminal differentiation requires the integration of tissue-specific cues that lead to the emergence of unique tissue-specific cDC features (Bosteels et al., 2020; Sichien et al., 2017).

In the spleen, XCR1$^+$ cDC1s are a relatively homogenous population that excels at cross-presentation (den Haan et al., 2000; Lehmann et al., 2017; Schnorrer et al., 2006). In contrast, Sirpα$^+$ cDC2s, which preferentially prime CD4$^+$ T cells, are phenotypically, transcriptionally, and functionally heterogeneous (Dudziak et al., 2007; Lehmann et al., 2017; Vander Lugt et al., 2014). Two main cDC2 subsets can be distinguished, Sirpα$^+$CD4$^+$Esam$^+$ cDC2s, which play pivotal roles in T helper type 17 cell (Th17 cell) polarization (Lewis et al., 2011; Satpathy et al., 2013), and Sirpα$^+$CD4$^-$Esam$^-$ cDC2s, which appear to be specifically involved in Th2 cell fate decisions (Tussiwand et al., 2015). While the transcription factors involved in the commitment to these disparate cDC fates are partially known (Murphy

[1]Laboratory of Immunoregulation and Mucosal Immunology, VIB-UGhent Center for Inflammation Research, Ghent, Belgium; [2]Department of Internal Medicine and Pediatrics, Ghent University, Ghent, Belgium; [3]Howard Hughes Medical Institute and Department of Microbiology and Immunology, University of California, San Francisco, San Francisco, CA; [4]Division of Virology, Department of Microbiology and Immunology, Institute of Medical Science, University of Tokyo, Tokyo, Japan; [5]Data Mining and Modeling for Biomedicine, VIB Center for Inflammation Research, Ghent, Belgium; [6]Department of Applied Mathematics, Computer Science and Statistics, Ghent University, Ghent, Belgium; [7]Laboratory of Myeloid Cell Ontogeny and Functional Specialization, VIB Center for Inflammation Research, Ghent, Belgium; [8]Department of Biomedical Molecular Biology, Ghent University, Ghent, Belgium; [9]Infectious and Inflammatory Diseases Center, Sanford Burnham Prebys Medical Discovery Institute, La Jolla, CA; [10]Institut Pasteur, Microenvironment and Immunity Unit, Paris, France; [11]Institut National de la Santé et de la Recherche Médicale U1224, Paris, France; [12]Institut Pasteur, Innate Immunity Unit, Department of Immunology, Paris, France; [13]Institut National de la Santé et de la Recherche Médicale U1223, Paris, France; [14]Innate Pharma Research Laboratories, Innate Pharma, Marseille, France; [15]Aix Marseille University, Centre National de la Recherche Scientifique, Institut National de la Santé et de la Recherche Médicale, Centre d'Immunologie de Marseille-Luminy, Marseille, France; [16]Assistance Publique - Hôpitaux de Marseille, Hôpital de la Timone, Service d'Immunologie, Marseille-Immunopôle, Marseille, France; [17]Department of Microbiology, Immunology and Molecular Genetics, University of Texas Health Science Center at San Antonio, San Antonio, TX; [18]Laboratory of Cellular and Molecular Immunology, Vrij Universiteit Brussel, Brussels, Belgium; [19]Department of Pulmonary Medicine, Erasmus University Medical Center, Rotterdam, Netherlands.

*M. Vanderkerken, A.P. Baptista, and M. De Giovanni contributed equally to this paper; **A.V. Tumanov, C. De Trez, and B.N. Lambrecht contributed equally to this paper; Correspondence to Bart N. Lambrecht: bart.lambrecht@ugent.be; Antonio P. Baptista: antonio.baptista@irc.vib-ugent.be.

et al., 2016), the cellular and molecular signals that instruct their expression remain largely unidentified.

To date, two main signals have been identified that control cDC development and differentiation in the spleen. Delta-like 1 (DLL1)–Notch2 and lymphotoxin ($LT\alpha_1\beta_2$)–LTβ receptor (LTβR) interactions are required for the development and/or homeostasis of Sirpα$^+$CD4$^+$Esam$^+$ cDC2s (Abe et al., 2003; Briseño et al., 2018; Fasnacht et al., 2014; Kabashima et al., 2005; Lewis et al., 2011; Satpathy et al., 2013; Wang et al., 2005; Wu et al., 1999). Regarding the latter ligand-receptor pair, cDC intrinsic LTβR expression and signaling regulates local CD4$^+$ cDC2 proliferation (De Trez et al., 2008; Kabashima et al., 2005; Satpathy et al., 2013). While the origin of membrane-bound heterotrimeric $LT\alpha_1\beta_2$ seems to be hematopoietic (Wu et al., 1999), its precise source remains controversial. Using mixed chimeric systems, evidence was obtained that $LT\alpha_1\beta_2$-expressing B cells were critical in splenic cDC2 homeostasis (Kabashima et al., 2005). Other reports questioned whether the B cell requirement was direct since gross abnormalities in lymphoid tissue architecture are common to B cell– and $LT\alpha_1\beta_2$-deficient states, potentially leading to secondary defects in cDC homeostasis (Crowley et al., 1999; Moseman et al., 2012; Phan et al., 2009; Wu et al., 1999; Zindl et al., 2009).

$LT\alpha_1\beta_2$ is expressed by multiple hematopoietic cells. Among these, innate lymphoid cells (ILCs) might constitute an alternative source of ligand for cDC homeostasis (Vivier et al., 2018), as it is now well appreciated that ILCs and cDC communicate extensively. For example, cDC1-derived IL-12 activates ILC1s for early control of toxoplasma and viral infections (Klose et al., 2014; Weizman et al., 2017); cDC2-derived IL-23 activates ILC3s coordinating mucosal immunity against bacterial infections (Cella et al., 2009; Kinnebrew et al., 2012).

While the data highlighted above indicate unidirectional communication between cDCs and ILCs, in which the former instructs the function of the latter, they fostered the hypothesis of reverse communication events whereby ILCs could directly influence cDC development and/or homeostasis. In agreement with this hypothesis, we show here that Rorgt$^+$ ILC3s are a critical, nonredundant source of $LT\alpha_1\beta_2$ that regulates the size of the splenic cDC niche and the terminal differentiation of Sirpα$^+$CD4$^+$Esam$^+$ cDC2s.

Results and discussion

Splenic cDC development is temporally asynchronous

The splenic cDC compartment is highly heterogeneous, comprising multiple subsets that are not only transcriptionally and phenotypically diverse (Fig. 1 A) but also functionally distinct (den Haan et al., 2000; Dudziak et al., 2007; Sathe and Shortman, 2008; Schnorrer et al., 2006; Vander Lugt et al., 2014). To unravel the origin of such heterogeneity, we examined early developmental stages of the murine spleen. We noticed that the cDC compartment did not emerge fixed but matured over time. While cDC numbers steadily rose as mice aged and the spleen increased in size (Fig. 1 B, left), XCR1$^+$ cDC1 and Sirpα$^+$ cDC2 subsets did it at different rates (Fig. 1 B, middle). Indeed, the rate at which Sirpα$^+$CD4$^+$Esam$^+$ cDC2 numbers increased was so pronounced that the early over-representation of cDC1s quickly disappeared, giving place to a splenic cDC compartment dominated by the former cells, which seemed to arrive at its mature representation around post-natal day 21 (Fig. 1 B, right).

The perinatal period represents a critical window in development, in which the first microbial encounters set the stage for subsequent immune homeostasis and host–pathogen interactions (Gensollen et al., 2016). Hence, we hypothesized that microbial colonization could be responsible for the observed alterations in splenic cDC ratios. To test this hypothesis, we analyzed mice raised in germ-free conditions or under broad antibiotic treatment. Neither approach modified the numbers of cDCs isolated from spleens (Fig. 1 C), suggesting that microbial exposure has no/minimal impact on splenic cDC development.

Tissue cDCs develop in situ from bone marrow–derived pre-cDC precursors (Cabeza-Cabrerizo et al., 2019; Grajales-Reyes et al., 2015; Liu et al., 2009; Naik et al., 2007; Schlitzer et al., 2015). Given that cDC1 and cDC2 have different immediate precursors, Ly6G$^-$CD11c^{int}MHC-II$^-$Flt3L$^+$Sirpα^{int}SiglecH$^-$Ly6C$^-$ pre-cDC1s and Ly6G$^-$CD11c^{int}MHC-II$^-$Flt3L$^+$Sirpα^{int}SiglecH$^-$Ly6C$^+$ pre-cDC2s, respectively (Fig. 1 D; Schlitzer et al., 2015), we considered the hypothesis that the temporal evolution we observed in mature splenic cDCs resulted from changes in their upstream precursors. Analysis of pre-cDCs by flow cytometry in either bone marrow or spleen revealed only mild changes throughout our observation period (Fig. 1 D); as these did not coincide with the kinetics of mature cDCs, we suggest that changes neither in pre-cDC bone marrow output nor in splenic "infiltration" account for the final composition of the splenic cDC compartment.

Taken together, these data suggested that splenic cDC development was programmed within the spleen independently of inputs from the bone marrow or the microbiota. More importantly, it seemed that the intrasplenic capacity to support cDC development varied in time.

ILCs regulate splenic Sirpα$^+$CD4$^+$Esam$^+$ cDC2 development

cDCs display diverse phenotypes across and within tissues, suggesting significant tissue adaptation (Sichien et al., 2017). In this regard, it is noteworthy that cDC subsets are not randomly distributed but seem to localize to distinct niches in several tissues (Baptista et al., 2019; Calabro et al., 2016; Dudziak et al., 2007; Gatto et al., 2013; Gerner et al., 2012; Yi and Cyster, 2013). In the spleen, XCR1$^+$ cDC1s were distributed between the T cell area and the red pulp; Sirpα$^+$CD4$^-$Mgl2$^+$ cDC2s seemed to localize mostly to the red pulp; and Sirpα$^+$CD4$^+$Mgl2$^-$ cDC2s localized predominantly to the bridging channels entering the T cell area (Fig. 2 A). These observations raised the hypothesis that splenic cDC development could be regulated by intercellular communications events taking place in dedicated niches. To test this hypothesis, we looked into animals lacking diverse immune cell subsets. Analysis of *Rag2*$^{-/-}$ mice, which lack B and T cells, revealed a decrease in splenic cDC numbers that affected all subsets equally (Fig. 2 B); this phenotype was the result of B cell deficiency (Fig. S1 A). Surprisingly, analysis of *Rag2*$^{-/-}$ x γc$^{-/-}$ spleens, which in addition to B and T cell deficiency are also devoid of innate lymphocytes, revealed a further reduction in

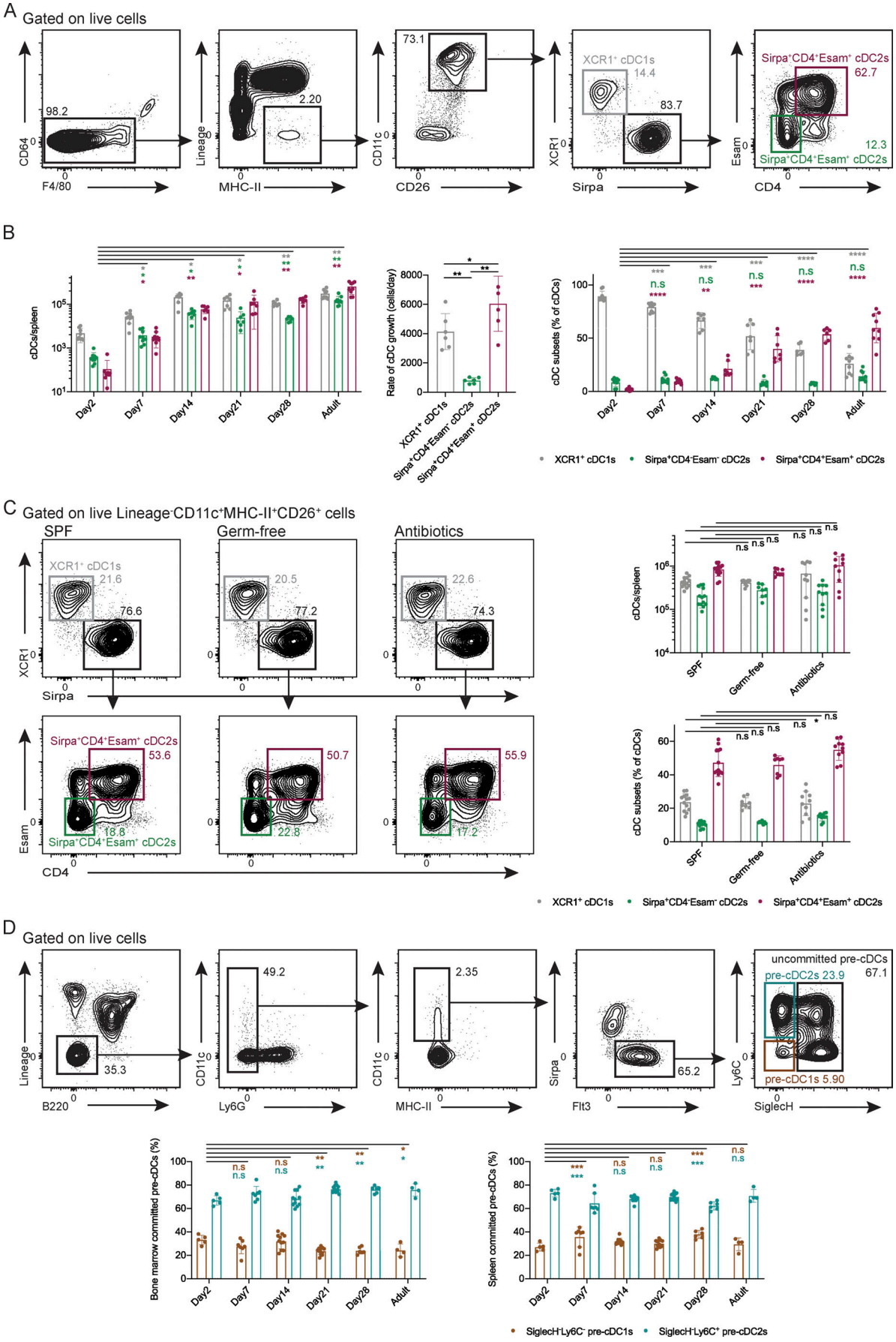
A
Gated on live cells
98.2
CD64
F4/80
2.20
Lineage
MHC-II
73.1
CD11c
CD26
XCR1⁺ cDC1s
14.4
83.7
XCR1
Sirpa
Sirpa⁺CD4⁺Esam⁺ cDC2s
62.7
12.3
Sirpa⁺CD4⁺Esam⁺ cDC2s
Esam
CD4
B
cDCs/spleen
Day2
Day7
Day14
Day21
Day28
Adult
Rate of cDC growth (cells/day)
XCR1⁺ cDC1s
Sirpa⁺CD4⁻Esam⁻ cDC2s
Sirpa⁺CD4⁺Esam⁺ cDC2s
cDC subsets (% of cDCs)
n.s
XCR1⁺ cDC1s
Sirpa⁺CD4⁻Esam⁻ cDC2s
Sirpa⁺CD4⁺Esam⁺ cDC2s
C
Gated on live Lineage⁻CD11c⁺MHC-II⁺CD26⁺ cells
SPF
Germ-free
Antibiotics
XCR1⁺ cDC1s
21.6
76.6
20.5
77.2
22.6
74.3
XCR1
Sirpa
Sirpa⁺CD4⁺Esam⁺ cDC2s
53.6
18.8
50.7
22.8
55.9
17.2
Esam
Sirpa⁺CD4⁺Esam⁺ cDC2s
CD4
cDCs/spleen
SPF
Germ-free
Antibiotics
cDC subsets (% of cDCs)
n.s
XCR1⁺ cDC1s
Sirpa⁺CD4⁻Esam⁻ cDC2s
Sirpa⁺CD4⁺Esam⁺ cDC2s
D
Gated on live cells
Lineage
B220
35.3
49.2
CD11c
Ly6G
2.35
CD11c
MHC-II
Sirpa
Flt3
65.2
uncommitted pre-cDCs
pre-cDC2s 23.9
67.1
Ly6C
pre-cDC1s 5.90
SiglecH
Bone marrow committed pre-cDCs (%)
Spleen committed pre-cDCs (%)
Day2
Day7
Day14
Day21
Day28
Adult
n.s
SiglecH⁻Ly6C⁻ pre-cDC1s
SiglecH⁻Ly6C⁺ pre-cDC2s

Figure 1. **The splenic cDC compartment matures asynchronously during early post-natal development. (A)** Representative flow-cytometric analysis for the identification and quantification of the different cDC subsets. cDCs are defined as CD64$^-$F4/80^{low}Lineage(CD3e/CD19/NK1.1/Ter119)$^-$MHC-II$^+$CD11c$^+$CD26$^+$ cells. **(B)** Quantification of WT splenic cDC subsets during early post-natal development. The number and frequency of the different subsets are both shown. The rate of cDC growth is calculated from the first 28 d of post-natal development. *n* = 9, day 2 samples; 9, day 7 samples; 7, day 14 samples; 7, day 21 samples; 6, day 28 samples; and 9 adult samples; data verified in at least two different experiments per time point; two-way ANOVA with Sidak's multiple comparisons post-test. **(C)** Representative flow cytometry plots and quantification of cDCs in the spleens of WT mice maintained in either SPF or germ-free conditions and in SPF mice treated with broad-spectrum antibiotics. *n* = 13 SPF mice, 8 germ-free mice, and 10 antibiotic-treated mice; at least two experiments per condition; two-way ANOVA with Sidak's multiple comparisons post-test. **(D)** Representative strategy for the identification of subset-committed pre-cDCs (a bone marrow sample is shown) by flow cytometry and quantification of pre-cDC1s and pre-cDC2s in the bone marrow and spleen of WT mice at different ages of post-natal development. Pre-cDCs are defined as Lineage(CD3e/CD19/NK1.1/Ter119)$^-$B220$^-$Ly6G$^-$CD11c$^+$Flt3$^+$Sirpα^{low} cells; committed pre-cDC1s are SiglecH$^-$Ly6C$^-$, whereas committed are pre-cDC2 SiglecH$^-$Ly6C$^+$. *n* = 5, day 2 samples; 7, day 7 samples; 11, day 14 samples; 13, day 21 samples; 6, day 28 samples; and 4 adult samples; data verified in at least two different experiments per time point; two-way ANOVA with Sidak's multiple comparisons post-test. *, P < 0.05; **, P < 0.01; ***, P < 0.001; ****, P < 0.0001.

cDC numbers (Fig. 2 B). This reduction affected Sirpα$^+$CD4$^+$Esam$^+$ cDC2 specifically, leading to an unbalanced cDC compartment (Fig. 2 B). Overall, these data suggested that B cells provide a general niche and/or signal(s) that promote broad splenic cDC development, whereas innate lymphocytes may be specifically required for the development and/or homeostasis of Sirpα$^+$CD4$^+$Esam$^+$ cDC2s.

To establish which type of innate lymphocytes, cytotoxic natural killer (NK) cells versus helper ILCs, promoted splenic Sirpα$^+$CD4$^+$Esam$^+$ cDC2 development, we took advantage of depleting antibodies. Whereas administration of anti-NK1.1 antibodies effectively depleted NK cells, leaving the ILC compartment intact, anti-CD90 antibodies had the opposite effect, eliminating Tbet$^+$ ILC1s, Gata3$^+$ ILC2s, and Rorgt$^+$ ILC3s efficiently while leaving NK cells untouched (Fig. S1, B and C). Depletion of NK cells had no effect on splenic cDCs (Fig. 2 C), a finding further confirmed in *NKp46*-Cre-DTA transgenic mice that in addition to NK cell deficiency also exhibited partial deficiencies in Tbet$^+$NKp46$^+$ ILC1s and Rorgt$^+$CD4$^-$NKp46$^+$ ILC3s (Fig. S1 D). In contrast, depletion of ILCs led to a specific reduction in the number of Sirpα$^+$CD4$^+$Esam$^+$ cDC2s (Fig. 2 C). These data suggested that ILCs, rather than NK cells, were required for proper development/homeostasis of Sirpα$^+$CD4$^+$Esam$^+$ cDC2s. To determine whether ILCs were also sufficient, we proceeded to reconstitute CD45.2$^+$ *Rag2*$^{-/-}$ x *γc*$^{-/-}$ mice with ILCs sorted from CD45.1$^+$ *Rag2*$^{-/-}$ congenic mice. 2 wk after adoptive transfer, low numbers of donor-derived ILCs could be readily recovered from the spleen of acceptor mice (Fig. 2 D), correlating with increased retrieval of Sirpα$^+$CD4$^-$Esam$^-$ and Sirpα$^+$CD4$^+$Esam$^+$ cDC2s (Fig. 2 E). cDC1s remained unaffected (Fig. 2 E). Of note, in these experiments, all ILC subsets increased concomitantly, precluding an accurate inference as to which ILC subset could be implicated in the homeostasis of Sirpα$^+$CD4$^+$Esam$^+$ cDC2s as all seemed to dose-dependently influence the relatively small but consistent restoration of this cDC2 compartment (Fig. S1 E). Taken together, our data suggest that ILCs (possibly in an ILC subset–specific manner) are necessary and partly sufficient for the homeostasis of splenic Sirpα$^+$CD4$^+$Esam$^+$ cDC2s.

Sirpα$^+$CD4$^+$Esam$^+$ cDC2 development requires ILC3s

To identify which ILC subset(s) was involved in Sirpα$^+$CD4$^+$Esam$^+$ cDC2 development and/or homeostasis, we combined immunostaining, confocal microscopy, and histocytometry (Gerner et al., 2012) to simultaneously assess ILC and cDC spatial distribution (Fig. 3 A). Early analysis showed that ILC subsets were unevenly distributed throughout the spleen. In particular, NK1.1$^+$Eomes$^-$ ILC1s and Gata3$^+$ ILC2s localized to the red pulp, whereas Rorgt$^+$ ILC3s were present mostly in bridging channels (Fig. S2 A). These observations suggested that Rorgt$^+$ ILC3s and Sirpα$^+$CD4$^+$ cDC2s were enriched in identical locations and, indeed, intimate contacts between the two cell types could be observed (Fig. 3 A; Hoorweg et al., 2015; Kim et al., 2007; Magri et al., 2014). To formally quantify these observations, we treated the records of intrasplenic ILC and cDC subset localization (Fig. 3 B) as multitype spatial point patterns for the purpose of statistical analysis. First, we calculated the nearest neighbor distance between all ILC and cDC subsets. These analyses revealed that, on average, Rorgt$^+$ ILC3s and Sirpα$^+$CD4$^+$ cDC2s resided in closer proximity to each other than any other ILC–cDC pair (Fig. 3 C and Fig. S2 B). Considering, however, that the proportions of the different cellular subsets were very different and this could bias our results, we took an in silico approach to "regress out" the influence of an overabundant Sirpα$^+$CD4$^+$ cDC2 compartment by sampling at random a number of Sirpα$^+$CD4$^+$ cDC2s equivalent to the least represented cDC subset in our datasets. Remeasuring the nearest neighbor distances showed that, after controlling for differences in cDC abundance, Rorgt$^+$ ILC3s still resided closer to Sirpα$^+$CD4$^+$ cDC2s than to any other cDC subset (Fig. S2 C). To further validate these findings, we compared our results to a random permutation null hypothesis where ILC labels, at their observed representation, were shuffled across their positional coordinates. As illustrated in Fig. S2 D, this strategy eliminated the preferential enrichment between Rorgt$^+$ ILC3s and Sirpα$^+$CD4$^+$ cDC2s in two out of three samples analyzed. Taken together, these analyses suggested that the spatial codistribution pattern of Rorgt$^+$ ILC3s and Sirpα$^+$CD4$^+$ cDC2s could not have emerged by chance alone. Hence, to gain further insight into the spatial cDC organization potentially promoted by Rorgt$^+$ ILC3s, we took Rorgt$^+$ ILC3s as points of origin from which the probabilities of observing cDCs of a given subset were calculated as a function of spatial two-dimensional distance. As before, these probabilities were compared with a random permutation null hypothesis by relabeling of ILCs. While Sirpα$^-$ cDC1s and Sirpα$^+$CD4$^-$ cDC2s exhibited a tendency to be segregated away from Rorgt$^+$ ILC3s, statistically this

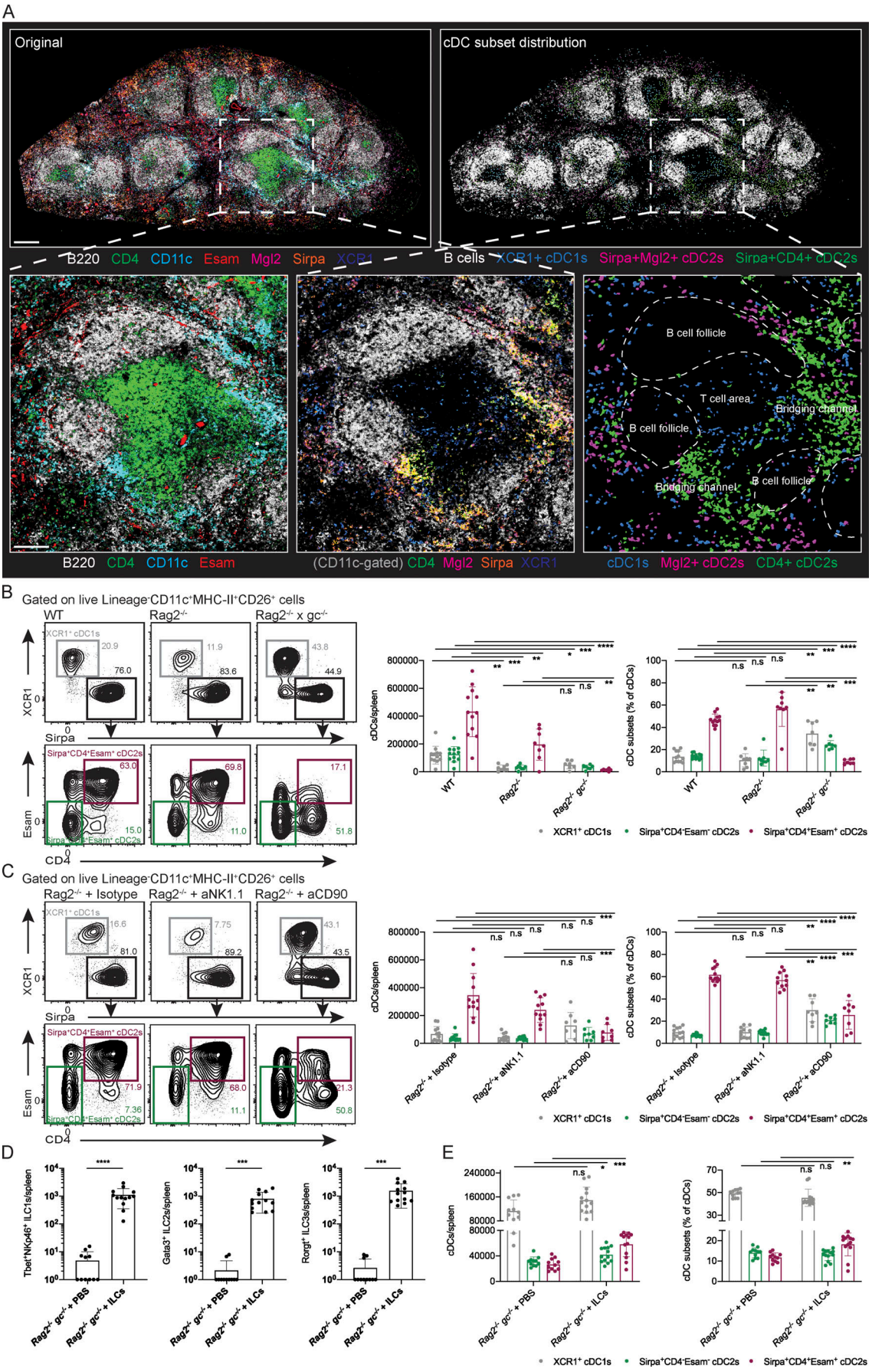
A
Original
cDC subset distribution
B220 CD4 CD11c Esam Mgl2 Sirpa XCR1
B cells XCR1+ cDC1s Sirpa+Mgl2+ cDC2s Sirpa+CD4+ cDC2s
B cell follicle
T cell area
Bridging channel
B cell follicle
Bridging channel
B cell follicle
B220 CD4 CD11c Esam
(CD11c-gated) CD4 Mgl2 Sirpa XCR1
cDC1s Mgl2+ cDC2s CD4+ cDC2s
B
Gated on live Lineage-CD11c+MHC-II+CD26+ cells
WT
Rag2-/-
Rag2-/- x gc-/-
XCR1+ cDC1s
20.9
76.0
11.9
83.6
43.8
44.9
XCR1
Sirpa
Sirpa+CD4+Esam+ cDC2s
63.0
15.0
69.8
11.0
17.1
51.8
Esam
CD4
cDCs/spleen
cDC subsets (% of cDCs)
WT
Rag2-/-
Rag2-/- gc-/-
XCR1+ cDC1s
Sirpa+CD4-Esam- cDC2s
Sirpa+CD4+Esam+ cDC2s
C
Gated on live Lineage-CD11c+MHC-II+CD26+ cells
Rag2-/- + Isotype
Rag2-/- + aNK1.1
Rag2-/- + aCD90
XCR1+ cDC1s
16.6
81.0
7.75
89.2
43.1
43.5
XCR1
Sirpa
Sirpa+CD4+Esam+ cDC2s
71.9
7.36
68.0
11.1
21.3
50.8
Esam
CD4
cDCs/spleen
cDC subsets (% of cDCs)
Rag2-/- + Isotype
Rag2-/- + aNK1.1
Rag2-/- + aCD90
XCR1+ cDC1s
Sirpa+CD4-Esam- cDC2s
Sirpa+CD4+Esam+ cDC2s
D
Tbet+NKp46+ ILC1s/spleen
Gata3+ ILC2s/spleen
Rorgt+ ILC3s/spleen
Rag2-/- gc-/- + PBS
Rag2-/- gc-/- + ILCs
E
cDCs/spleen
cDC subsets (% of cDCs)
Rag2-/- gc-/- + PBS
Rag2-/- gc-/- + ILCs
XCR1+ cDC1s
Sirpa+CD4-Esam- cDC2s
Sirpa+CD4+Esam+ cDC2s

Figure 2. **The terminal differentiation of Sirpα⁺CD4⁺Esam⁺ cDC2s requires ILCs. (A)** Representative immunofluorescence image of WT splenic cDCs. Spleen sections were stained with the indicated markers, allowing identification of the major anatomical regions and cDC subsets. CD11c⁺ voxels were used to mask cDC-specific markers and to create the surface renderings that are plotted on top of anatomically demarcated regions. Esam staining demarcated vessels and the marginal zone, but expression on DCs was too low for accurate quantification. *n* = 4 spleens. Scale bars, 200 µm for low-magnification images, 100 µm for insets. **(B)** Representative flow cytometry plots and quantification of splenic cDCs in WT, *Rag2*$^{-/-}$, and *Rag2*$^{-/-}$ x *γc*$^{-/-}$ mice. *n* = 12 WT mice, 8 *Rag2*$^{-/-}$ mice, and 7 *Rag2*$^{-/-}$ x *γc*$^{-/-}$ mice; three independent experiments; two-way ANOVA with Sidak's multiple comparisons post-test. **(C)** Representative flow cytometry plots and quantification of splenic cDCs in *Rag2*$^{-/-}$ treated with depleting NK1.1 or CD90 antibodies. *n* = 12 *Rag2*$^{-/-}$ + isotype antibody control mice, 11 *Rag2*$^{-/-}$ + aNK1.1 mice, and 8 *Rag2*$^{-/-}$ + aCD90 mice; at least two independent experiments per treatment regimen; two-way ANOVA with Sidak's multiple comparisons post-test. **(D and E)** Number of ILCs (D) and cDCs (E) recovered from the spleens of *Rag2*$^{-/-}$ x *γc* $^{-/-}$ mice, 14 d after adoptive transfer. *n* = 11 *Rag2*$^{-/-}$ x *γc* $^{-/-}$ PBS control mice, 13 *Rag2*$^{-/-}$ x *γc*$^{-/-}$ + ILCs; three independent experiments; Mann–Whitney *U* test in D; two-way ANOVA with Sidak's multiple comparisons post-test in E. *, P < 0.05; **, P < 0.01; ***, P < 0.001; ****, P < 0.0001.

seemed to occur by chance. In contrast, Sirpα⁺CD4⁺ cDC2s exhibited a higher probability of being near Rorgt⁺ ILC3s than would be expected (Fig. 3 D and Fig. S2 E). Taken together, these data suggested that ILC3s and Sirpα⁺CD4⁺Esam⁺ cDC2s may engage in bi-directional communication in vivo.

To probe whether the differentiation of Sirpα⁺CD4⁺Esam⁺ cDC2s depended on ILC3s, as the prior data suggested, we analyzed spleens from *Rorc*$^{GFP/GFP}$ mice. In these mice, the presence of two copies of the *Rorc*-GFP transgene results in constitutive Rorgt deficiency, impairing ILC3 development (Eberl et al., 2004). As compared with *Rorc*$^{+/+}$ and *Rorc*$^{GFP/+}$ littermate controls, *Rorc*$^{GFP/GFP}$ mice exhibited reduced numbers of Sirpα⁺CD4⁺Esam⁺ cDC2s (Fig. 3 E). In this experimental setup, in which B cells are present in normal numbers, XCR1⁺ cDC1 and Sirpα⁺CD4⁻Esam⁻ cDC2 homeostasis remained unaffected (Fig. 3 E). Identical results were obtained in *Rag2*$^{-/-}$ x *Rorc*$^{GFP/GFP}$ mice, in which deletion of ILC3s incremented Sirpα⁺CD4⁺Esam⁺ cDC2 deficiency without affecting XCR1⁺ cDC1 and Sirpα⁺CD4⁻Esam⁻ cDC2 numbers (Fig. 3 F). Combined, these results suggested that ILC3s specifically regulate Sirpα⁺CD4⁺Esam⁺ cDC2 homeostasis in both lymphoreplete and lymphopenic environments. However, given that the reduction in Sirpα⁺CD4⁺Esam⁺ cDC2 numbers was much more pronounced in Rag2-deficient as compared with Rag2-sufficient mice, i.e., in the absence versus the presence of B cells, it seems that some degree of compensation for ILC3 deficiency may be exerted by Rag2-dependent B cells.

Sirpα⁺CD4⁺Esam⁺ cDC2 development requires ILC3-derived LTα$_1$β$_2$

The preceding data revealed a specific role for ILC3s in the regulation of splenic Sirpα⁺CD4⁺Esam⁺ cDC2 homeostasis. To identify candidates mediating the intercellular communication events between ILC3s and Sirpα⁺CD4⁺Esam⁺ cDC2s responsible for the maintenance of the latter cells, we took a computational approach (Fig. 4 A). First, we screened publicly available transcriptional profiles of splenic cDCs (Brown et al., 2019) to identify differentially expressed genes between the three cDC subsets. As depicted in Fig. 4 B, in which individual genes are plotted as points in a hexagonal diagram containing three axes (one per cDC subset) placed at 120° angles, and where the distances to the center and angle represent the log$_2$ fold induction and the directionality of such induction, respectively, differentially expressed genes overpopulated the horizontal axis representing the global comparison XCR1⁺ cDC1s versus CD11b⁺ (Sirpα⁺) cDC2s. These data, which are further highlighted in the adjacent rose plots depicting the percentage of differentially expressed genes, are consistent with a major bifurcation between cDC1 and cDC2 development as previously demonstrated (Ma et al., 2019; Schlitzer et al., 2015). Comparatively, Tbet⁻ (Sirpα⁺CD4⁻Esam⁻) cDC2s and Tbet⁺ (Sirpα⁺CD4⁺Esam⁺) cDC2s were closer to each other. Inspection of the genes specifically associated with Tbet⁺ (Sirpα⁺CD4⁺Esam⁺) cDC2s revealed the presence of several modules related to leukocyte differentiation and intercellular communication (signaling and cell–cell adhesion; Fig. 4 C). This result prompted the use of NicheNet (Browaeys et al., 2020), an algorithm capable of inferring the ligand–receptor interactions occurring between cellular pairs by combining transcriptome data of the interacting cells with a priori knowledge on signaling and gene regulatory networks. Specifically, we applied NicheNet to infer which ligand–receptor pairs expressed by Rorgt⁺ ILC3s and Tbet⁺ (Sirpα⁺CD4⁺Esam⁺) cDC2s could regulate the expression of the Tbet⁺ cDC2–associated genes found. Among the top predicted ligands expressed by ILC3s that could induce the Tbet⁺ cDC2 gene signature (Fig. 4 D), two signals known to affect splenic cDC homeostasis were present, *Dll1* (Fasnacht et al., 2014; Lewis et al., 2011) and *Lta* (Abe et al., 2003; Kabashima et al., 2005; Wang et al., 2005; Wu et al., 1999). Of note, while *Ltb* did not appear in the top 20 predicted ligands, it was also present in the list of predicted ligands produced by NicheNet, and moreover, it was highly expressed by ILC3s (Björklund et al., 2016; Gury-BenAri et al., 2016; Magri et al., 2014; Reboldi et al., 2016). Hence, on the basis of absolute ligand and receptor expression on ILC3s and Tbet⁺ cDC2s, respectively (Fig. 4 D), and of the known biology of ILC3s (van de Pavert and Mebius, 2010), we hypothesized that ILC3-derived LTα$_1$β$_2$ was responsible for Sirpα⁺CD4⁺Esam⁺ cDC2 maintenance.

In support of our hypothesis, we found that cDC2s from *Rag2*$^{-/-}$ and *Rag2*$^{-/-}$ x *γc*$^{-/-}$ mice expressed higher levels of LTβR as compared with WT cDC2s (Fig. 4 E); comparatively, LTβR levels on cDC1s were minorly affected (Fig. 4 E). This increase in receptor expression, which was more pronounced as the degree of Sirpα⁺CD4⁺Esam⁺ cDC2 deficits increased, may represent lack of ligand-induced receptor down-regulation (Kabashima et al., 2005; Lewis et al., 2011; Yi and Cyster, 2013). Most crucially, this observation simultaneously suggested that ILC3s and cDC2s communicate via LTα$_1$β$_2$ and that LTα$_1$β$_2$ signaling regulates Sirpα⁺CD4⁺Esam⁺ cDC2 homeostasis. Consistently, we observed that treatment of mice with LTβR Fc fusion antagonist (LTβR-Fc), a decoy receptor that blocks the biological activity of LTα$_1$β$_2$,

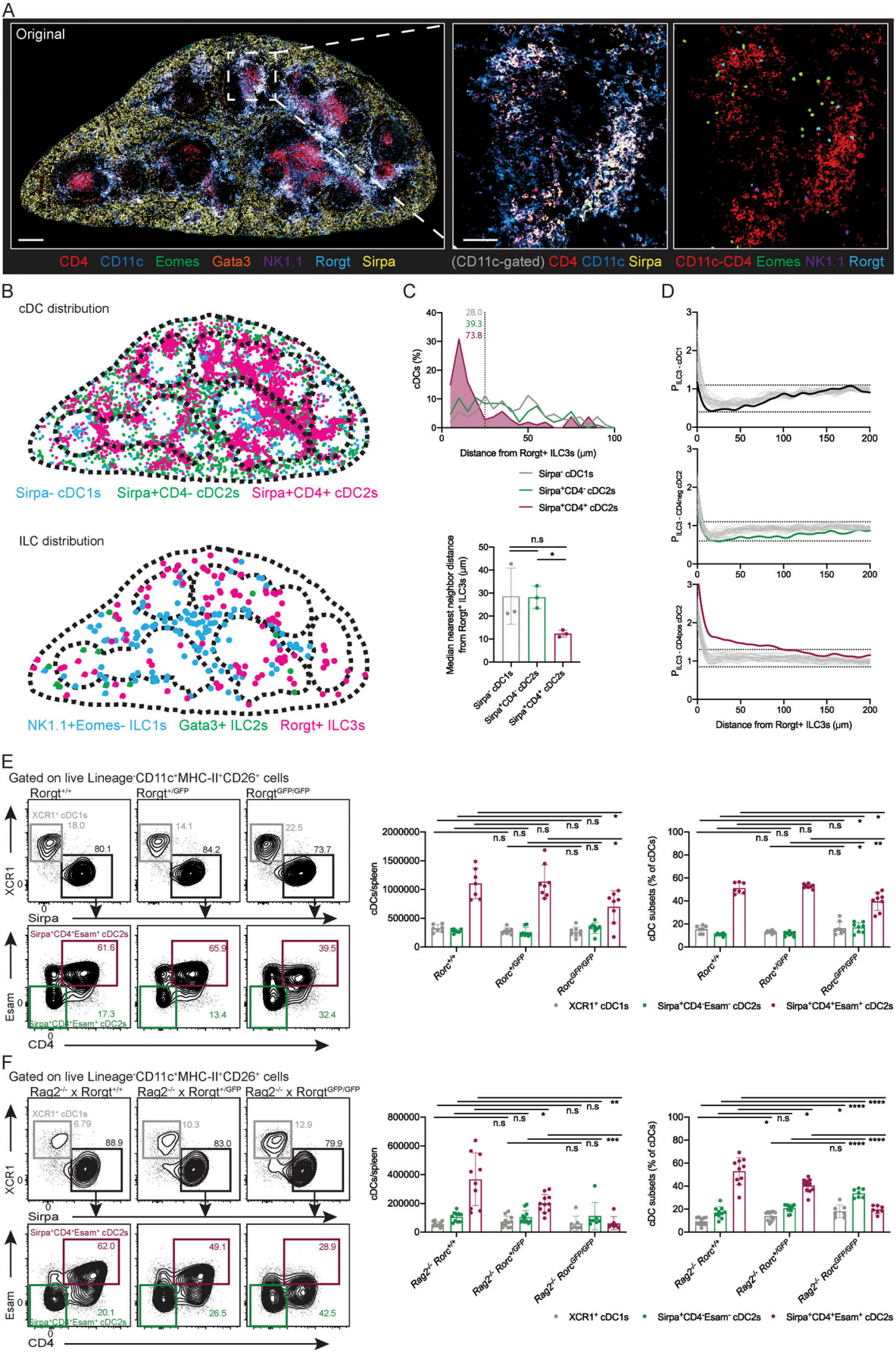
A
Original
CD4 CD11c Eomes Gata3 NK1.1 Rorgt Sirpa
(CD11c-gated) CD4 CD11c Sirpa
CD11c-CD4 Eomes NK1.1 Rorgt
B
cDC distribution
Sirpa- cDC1s Sirpa+CD4- cDC2s Sirpa+CD4+ cDC2s
ILC distribution
NK1.1+Eomes- ILC1s Gata3+ ILC2s Rorgt+ ILC3s
C
cDCs (%)
Distance from Rorgt+ ILC3s (μm)
Sirpa- cDC1s
Sirpa+CD4- cDC2s
Sirpa+CD4+ cDC2s
Median nearest neighbor distance from Rorgt+ ILC3s (μm)
n.s
D
PILC3 -cDC1
PILC3 - CD4neg cDC2
PILC3 - CD4pos cDC2
Distance from Rorgt+ ILC3s (μm)
E
Gated on live Lineage-CD11c+MHC-II+CD26+ cells
Rorgt+/+
Rorgt+/GFP
RorgtGFP/GFP
XCR1+ cDC1s
Sirpa+CD4+Esam+ cDC2s
Sirpa+CD4-Esam- cDC2s
XCR1
Sirpa
Esam
CD4
cDCs/spleen
cDC subsets (% of cDCs)
Rorc+/+
Rorc+/GFP
RorcGFP/GFP
XCR1+ cDC1s
Sirpa+CD4-Esam- cDC2s
Sirpa+CD4+Esam+ cDC2s
F
Gated on live Lineage-CD11c+MHC-II+CD26+ cells
Rag2-/- x Rorgt+/+
Rag2-/- x Rorgt+/GFP
Rag2-/- x RorgtGFP/GFP
Rag2-/- Rorc+/+
Rag2-/- Rorc+/GFP
Rag2-/- RorcGFP/GFP
XCR1+ cDC1s
Sirpa+CD4-Esam- cDC2s
Sirpa+CD4+Esam+ cDC2s

Figure 3. **Rorgt⁺ ILC3s nonredundantly control the homeostasis of Sirpα⁺CD4⁺Esam⁺ cDC2s. (A)** Representative immunofluorescence image of WT splenic cDCs and ILCs. Spleen sections were stained with the indicated markers allowing identification of the different cDC and ILC subsets. CD11c⁺ voxels were used to mask cDC-specific markers as shown in the middle panel. ILC subsets were identified based on the expression of Eomes, Gata3, NK1.1, and Rorgt. Note also the presence, in the right panel, of Eomes⁺NK1.1⁻ cells that most likely represent regulatory T cells. *n* = 3 spleens. Scale bars, 200 µm for low-magnification images, 100 µm for insets. **(B)** Schematic representation of cDC and ILC subset distribution in the spleen shown in A. **(C)** Spatial frequency distribution of WT cDCs around Rorgt⁺ ILC3s for the spleen shown in A. The numbers on the plot reflect the percentage of cDCs from each subset present in a 25-µm radius from Rorgt⁺ ILC3s. Bottom: Summary of median nearest neighbor distance for the three spleens analyzed. Repeated-measures ANOVA with Tukey's multiple comparisons post-test. **(D)** Probability of observing a cDC of a given subset as a function of spatial distance from Rorgt⁺ ILC3s in the spleen shown in A. The observed probability is shown in bold. The result of randomly relabeling Rorgt⁺ ILC3s across the ILC repertoire is show in gray (*n* = 39). The upper and lower boundary values for those simulations are depicted by the dotted lines. **(E)** Representative flow cytometry plots and quantification of splenic cDCs in *Rorc*$^{+/+}$, *Rorc*$^{GFP/+}$, and *Rorc*$^{GFP/GFP}$ mice. *n* = 7 *Rorc*$^{+/+}$ mice, 8 *Rorc*$^{GFP/+}$ mice, and 8 *Rorc*$^{GFP/GFP}$ mice; two independent experiments; two-way ANOVA with Sidak's multiple comparisons post-test. **(F)** Representative flow cytometry plots and quantification of splenic cDCs in *Rag2*$^{-/-}$ x *Rorc*$^{+/+}$, *Rag2*$^{-/-}$ x *Rorc*$^{GFP/+}$ and *Rag2*$^{-/-}$ x *Rorc*$^{GFP/GFP}$ mice. *n* = 10 *Rag2*$^{-/-}$ x *Rorc*$^{+/+}$ mice, 11 *Rag2*$^{-/-}$ x *Rorc*$^{GFP/+}$ mice, and 7 *Rag2*$^{-/-}$ x *Rorc*$^{GFP/GFP}$ mice; three independent experiments; two-way ANOVA with Sidak's multiple comparisons post-test. *, P < 0.05; **, P < 0.01; ***, P < 0.001; ****, P < 0.0001.

specifically reduced Sirpα⁺CD4⁺Esam⁺ cDC2 numbers (Fig. 4 F and Fig. S3 A); conversely, treatment of *Rag2*$^{-/-}$ x *γc*$^{-/-}$ mice with an agonistic LTβR antibody distinctively restored this cDC compartment (Figs. 4 G and Fig. S3 B). Given that LTβR-Fc treatment reduced Sirpα⁺CD4⁺Esam⁺ cDC2 numbers in WT and *Rag2*$^{-/-}$ but not *Rag2*$^{-/-}$ x *γc*$^{-/-}$ mice (Fig. 4 F), combined these experiments implicated $LT\alpha_1\beta_2$ signaling as a crucial regulator of Sirpα⁺CD4⁺Esam⁺ cDC2 homeostasis and revealed adaptive and innate lymphocytes as the critical sources of such signals.

By studying mice with B cell–specific transgenic overexpression of $LT\alpha_1\beta_2$ and mice with *μMT:Ltα*$^{-/-}$ mixed bone marrows, we have previously shown a critical role for B cell–derived $LT\alpha_1\beta_2$ in splenic cDC2 homeostasis (Kabashima et al., 2005); these effects might have been indirect and caused by a defect in lymph node architecture (Crowley et al., 1999; Moseman et al., 2012; Zindl et al., 2009). Hence, to conclusively examine whether ILC3s mediated Sirpα⁺CD4⁺Esam⁺ cDC2 homeostasis via $LT\alpha_1\beta_2$ and distinguish between the function of B cell– and ILC3-derived $LT\alpha_1\beta_2$ in a cell-intrinsic manner, we combined *Ltb*^{flox} alleles with *Cd19*-Cre and/or *Rorc*-Cre transgenes. The resulting mice lacked LTβ expression on B cells (*Cd19*-Cre; Tumanov et al., 2002), ILC3s and T cells (*Rorc*-Cre; Kruglov et al., 2013) or both (*Cd19*-Cre x *Rorc*-Cre). Analysis of their spleens revealed that LTβ expression on B cells and ILC3s independently regulated the size of the splenic cDC compartment. Both B cell and ILC3 LTβ deficiency induced significant reductions in XCR1⁺ cDC1, Sirpα⁺CD4⁻Esam⁻ cDC2, and Sirpα⁺CD4⁺Esam⁺ cDC2 numbers (Fig. 4 H and Fig. S3 C). Combined B cell and ILC3 LTβ deficiency caused a further contraction specifically in Sirpα⁺CD4⁺Esam⁺ cDC2 numbers (Fig. 4 H and Fig. S3 C). Taken together, these results suggest that $LT\alpha_1\beta_2$ signals with origin in B cells and ILC3s additively (or synergistically) regulate the splenic cDC niche size. Albeit smaller, the resulting niche in *Ltb*$^{flox/flox}$ x *Cd19*-Cre and *Ltb*$^{flox/flox}$ x *Rorc*-Cre mice seems to adequately support Sirpα⁺CD4⁺Esam⁺ cDC2 differentiation. This process becomes adversely affected only when neither B cells nor ILC3s (*Ltb*$^{flox/flox}$ x *Cd19*-Cre x *Rorc*-Cre mice) can provide $LT\alpha_1\beta_2$. Consistent with this latter finding and thus multiple sources of $LT\alpha_1\beta_2$, treatment of *uMT*$^{-/-}$ mice with LTβR-Fc provoked a specific reduction in splenic Sirpα⁺CD4⁺Esam⁺ cDC2 numbers (Fig. S3 D). Although *Ltb*$^{flox/flox}$ x *Rorc*-Cre mice lack LTβ in both ILC3s and T cells (Kruglov et al., 2013), the role of T cell–derived LTβ in cDC2s homeostasis seems not essential compared with ILC3-derived LTβ, as *Rag2*$^{-/-}$ and *uMT*$^{-/-}$ mice had similar phenotypes and LTβR-Fc treatment effectively reduced splenic Sirpα⁺CD4⁺Esam⁺ cDC2 numbers in *Rag2*$^{-/-}$, but not *Rag2*$^{-/-}$ x *γc*$^{-/-}$, mice (Fig. 4 F).

Our data show a synergistic role of $LT\alpha_1\beta_2$ expressed on ILC3s and B cells in splenic cDC2 homeostasis. Whereas $LT\alpha_1\beta_2$-expressing B cells are numerous in the spleen, $LT\alpha_1\beta_2$-expressing ILC3s are relatively scant (Schaeuble et al., 2017). While this disparity probably explains why B cells seem to have a bigger cumulative influence in splenic cDC homeostasis as compared with ILC3s, it also suggests that, at the single-cell level, $LT\alpha_1\beta_2$-expressing ILC3s might be more potent regulators of the splenic cDC compartment. Consistently, in various tissues, ILC3s are known to express significantly higher levels of $LT\alpha_1\beta_2$ as compared with B cells (Björklund et al., 2016; Gury-BenAri et al., 2016; Magri et al., 2014; Reboldi et al., 2016). Alternatively, it may be that by acting during embryogenesis in the promotion of lymphoid tissue development (van de Pavert and Mebius, 2010), ILC3s, which include lymphoid tissue inducer cells, affect the ability of B cells to communicate with developing cDC and thus secondarily limit the provision of B cell–derived $LT\alpha_1\beta_2$. In favor of this hypothesis, combined LTβ deficiency in B cells and ILC3s indeed does not grossly increase the deficits in cDC1s and Sirpα⁺CD4⁺Esam⁻ cDC2s observed in either B cell– or ILC3-specific LTβ-deficient hosts, and neither LTβR blockade nor agonism in adulthood is able to influence the numbers of these two cDC subsets. These observations imply that the splenic cDC niche is formed early on and requires $LT\alpha_1\beta_2$ signals provided by both ILC3s and B cells that act on the same developmental pathway without built-in redundancy. Once formed, however, the cDC niche becomes $LT\alpha_1\beta_2$-insensitive.

In contrast to this temporally restricted prerequisite, Sirpα⁺CD4⁺Esam⁺ cDC2s required $LT\alpha_1\beta_2$ continuously as numbers of these cells were influenced by both LTβR blockade and LTβR agonism well into adulthood. Whereas also here B cells and ILC3s seemed to be the major providers of $LT\alpha_1\beta_2$, no single source seemed essential, and both cells were capable of compensating for the lack of the other.

In *Rag2*$^{-/-}$ x *γc*$^{-/-}$, *Rag2*$^{-/-}$ x *Rorc*$^{GFP/GFP}$, and *Ltb*$^{flox/flox}$ x *Cd19*-Cre x *Rorc*-Cre mice, residual numbers of Sirpα⁺CD4⁺Esam⁺

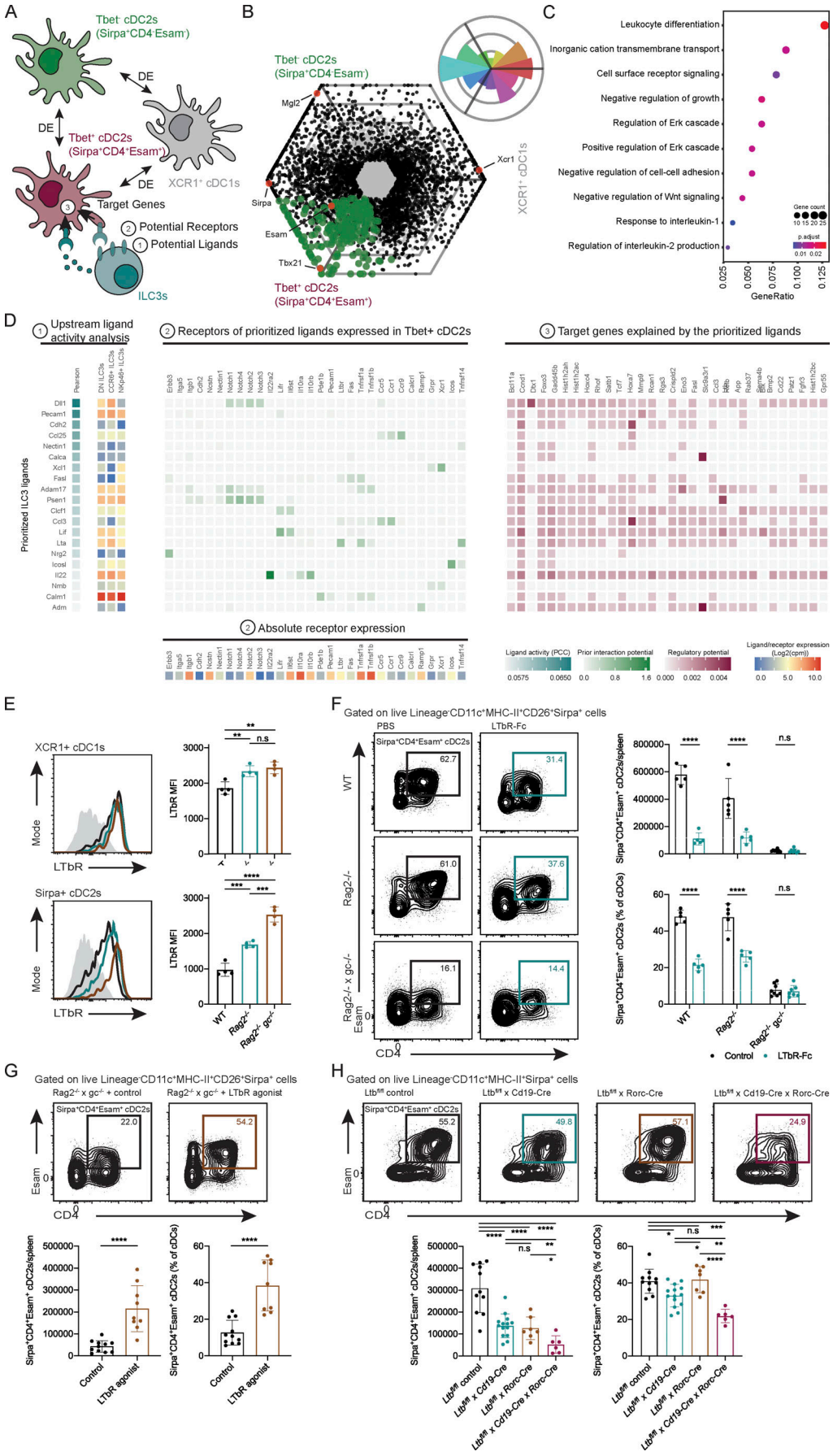
A
Tbet⁻ cDC2s (Sirpa⁺CD4⁻Esam⁻)
DE
Tbet⁺ cDC2s (Sirpa⁺CD4⁺Esam⁺)
XCR1⁺ cDC1s
Target Genes
Potential Receptors
Potential Ligands
ILC3s
B
Tbet⁻ cDC2s (Sirpa⁺CD4⁻Esam⁻)
Mgl2
Xcr1
XCR1⁺ cDC1s
Sirpa
Esam
Tbx21
Tbet⁺ cDC2s (Sirpa⁺CD4⁺Esam⁺)
C
Leukocyte differentiation
Inorganic cation transmembrane transport
Cell surface receptor signaling
Negative regulation of growth
Regulation of Erk cascade
Positive regulation of Erk cascade
Negative regulation of cell-cell adhesion
Negative regulation of Wnt signaling
Response to interleukin-1
Regulation of interleukin-2 production
Gene count
p.adjust
GeneRatio
D
1 Upstream ligand activity analysis
2 Receptors of prioritized ligands expressed in Tbet+ cDC2s
3 Target genes explained by the prioritized ligands
Prioritized ILC3 ligands
2 Absolute receptor expression
Ligand activity (PCC)
Prior interaction potential
Regulatory potential
Ligand/receptor expression (Log2(cpm))
E
XCR1+ cDC1s
Mode
LTbR
Sirpa+ cDC2s
LTbR MFI
WT
Rag2-/-
Rag2-/- gc-/-
F
Gated on live Lineage⁻CD11c⁺MHC-II⁺CD26⁺Sirpa⁺ cells
PBS
LTbR-Fc
Sirpa⁺CD4⁺Esam⁺ cDC2s
62.7
31.4
61.0
37.6
16.1
14.4
Esam
CD4
Sirpa⁺CD4⁺Esam⁺ cDC2s/spleen
Sirpa⁺CD4⁺Esam⁺ cDC2s (% of cDCs)
n.s
Control
LTbR-Fc
G
Gated on live Lineage⁻CD11c⁺MHC-II⁺CD26⁺Sirpa⁺ cells
Rag2-/- x gc-/- + control
Rag2-/- x gc-/- + LTbR agonist
22.0
54.2
Control
LTbR agonist
H
Gated on live Lineage⁻CD11c⁺MHC-II⁺Sirpa⁺ cells
Ltb^f/f control
Ltb^f/f x Cd19-Cre
Ltb^f/f x Rorc-Cre
Ltb^f/f x Cd19-Cre x Rorc-Cre
55.2
49.8
57.1
24.9

Figure 4. **LTα$_1$β$_2$-expressing Rorgt$^+$ ILC3s regulate Sirpα$^+$CD4$^+$Esam$^+$ cDC2 homeostasis. (A)** Schematic representation of the computational analysis performed to identify the ligand–receptor pairs potentially involved in intercellular ILC3-Tbet$^+$ (Sirpα$^+$CD4$^+$Esam$^+$) cDC2 communication. Differentially expressed (DE) genes between the different cDC subsets were identified; transcriptional data from ILC3s was integrated to infer potential ligands expressed by ILC3s (1), potential receptors expressed by Tbet$^+$ cDC2s (2), and the target genes of the identified ligand-receptor pairs among the DE genes in Tbet$^+$ cDC2s (3). **(B)** Hexagonal triwise plot depicting differentially expressed (black) and nondifferentially expressed (gray) genes between XCR1$^+$ cDC1s, Tbet$^-$ (Sirpα$^+$CD4$^-$Esam$^-$) cDC2s, and Tbet$^+$ (Sirpα$^+$CD4$^+$Esam$^+$) cDC2s; each new hexagon reflects a twofold difference from the previous with clipping at 32-fold. Highlighted in green are the genes belonging to the Tbet$^+$ (Sirpα$^+$CD4$^+$Esam$^+$) cDC2 gene signature. Highlighted in red are representative genes used throughout the paper to identify the different cDC subsets. The rose plot on the top right corner depicts the percentage of differentially expressed genes in each cellular direction; each circle represents a 5% increase. **(C)** Top 10 GO terms associated with the Tbet$^+$ (Sirpα$^+$CD4$^+$Esam$^+$) cDC2 gene signature. **(D)** NicheNet analysis of the ILC3-expressed ligands and Tbet$^+$ (Sirpα$^+$CD4$^+$Esam$^+$) cDC2-expressed receptors potentially involved in mediating intercellular communication events between the two cell types. The top 20 prioritized upstream ligands based on Tbet$^+$ cDC2 gene signature are shown in 1; in 2, the potential receptors associated with each ligand and expressed by Tbet$^+$ cDC2s are shown; and in 3, the potential target genes of the identified ligand–receptor pairs are highlighted. **(E)** Representative flow cytometry histograms and quantification of LTβR expression in splenic XCR1$^+$ cDC1s and Sirpα$^+$ cDC2s from WT, *Rag2*$^{-/-}$, and *Rag2*$^{-/-}$ x *γc*$^{-/-}$ mice. *n* = 4 mice/group; results from one representative experiment of two performed; Kruskal–Wallis test with Dunn's multiple comparisons post-test. MFI, mean fluorescence intensity. **(F)** Representative flow cytometry plots and quantification of splenic Sirpα$^+$CD4$^+$Esam$^+$ cDC2s in WT, *Rag2*$^{-/-}$ and *Rag2*$^{-/-}$ x *γc* $^{-/-}$ mice treated with the antagonist LTβR-Fc decoy receptor. *n* = 5 control + 5 LTβR-Fc-treated WT mice, 5 control + 5 LTβR-Fc-treated *Rag2*$^{-/-}$ mice, and 8 control + 7 LTβR-Fc-treated *Rag2*$^{-/-}$ x *γc*$^{-/-}$ mice; two independent experiments per genotype; two-way ANOVA with Sidak's multiple comparisons post-test. **(G)** Representative flow cytometry plots and quantification of splenic Sirpα$^+$CD4$^+$Esam$^+$ cDC2s in *Rag2*$^{-/-}$ x *γc* $^{-/-}$ mice treated with an agonist LTβR antibody. *n* = 11 *Rag2*$^{-/-}$ x *γc* $^{-/-}$ mice treated with control antibody, and 9 *Rag2*$^{-/-}$ x *γc*$^{-/-}$ mice treated with anti-LTβR; three independent experiments; Mann–Whitney *U* test. **(H)** Representative flow cytometry plots and quantification of splenic Sirpα$^+$CD4$^+$Esam$^+$ cDC2s in *Ltb*$^{flox/flox}$ control, *Ltb*$^{flox/flox}$ x *Cd19-Cre*, *Ltb*$^{flox/flox}$ x *Rorc-Cre,* and *Ltb*$^{flox/flox}$ x *Cd19-Cre* x *Rorc-Cre* mice. *n* = 11 *Ltb*$^{flox/flox}$ control, 15 *Ltb*$^{flox/flox}$ x *Cd19-Cre*, 7 *Ltb*$^{flox/flox}$ x *Rorc-Cre,* and 6 *Ltb*$^{flox/flox}$ x *Cd19-Cre* x *Rorc-Cre* mice; data verified in at least two independent experiments per genotype; Kruskal–Wallis test with Dunn's multiple comparisons post-test. *, P < 0.05; **, P < 0.01; ***, P < 0.001; ****, P < 0.0001.

cDC2s persist. Whether these cells are identical to those found in WT conditions or represent precursors arrested in their differentiation process due to lack of sufficient input from B cells and ILC3s remains to be determined. Importantly, however, these cells seemed to develop independently of LTα$_1$β$_2$ signaling as they were not only insensitive to LTβR-Fc treatment but also present in *Ltb*$^{-/-}$ mice (data not shown). Although we clearly found ILC3s and Sirpα$^+$CD4$^+$Esam$^+$ cDC2s to occupy the same spatial niche, the bridging channel, and illustrated how several ILC3-expressed molecules have the potential to modulate gene expression in cDC2s, an additional factor provided by non-lymphocytes hence seems to quick-start cDC2 differentiation. This factor is likely to be stromal cell–derived DLL1 (Fasnacht et al., 2014), as Notch2 and LTβR deletions seem to target the same cDC populations in spleen and small intestine (Briseño et al., 2018; Fasnacht et al., 2014; Lewis et al., 2011; Satpathy et al., 2013).

Splenic white pulp development requires LTα$_1$β$_2$ (Fu et al., 1998; Gonzalez et al., 1998; Kim et al., 2007; Ngo et al., 2001; Schaeuble et al., 2017; Tumanov et al., 2002). We have previously shown that LTβR expression in hematopoietic cells, rather than in radioresistant stromal cells, is essential for proper development of splenic CD4$^+$ cDC2s (De Trez et al., 2008). In those experiments, reconstitution of the CD4$^+$ cDC2 compartment occurred in spite of abrogated Ccl19, Ccl21, and Cxcl13 levels in LTβR-deficient recipients (De Trez et al., 2008). These results, which suggest at least partial independence between LTα$_1$β$_2$-mediated white pulp and cDC development, indicate that the traditional dichotomy between T cell area and B cell follicle stromal cells may not be at play in cDC development and thus raise the question as to how ILC3s and Sirpα$^+$CD4$^+$Esam$^+$ cDC2s come to localize in the same niche. Given our previous work and that of others, we speculate that the chemoattractant receptor Ebi2 might be implicated in this process. Ebi2 was shown to be involved both in the localization of ILC3s in intestinal cryptopatches and isolated lymphoid tissues (Chu et al., 2018; Emgård et al., 2018) and in cDC2 distribution in splenic bridging channels and the B cell follicle/T cell zone interface (Gatto et al., 2013; Lu et al., 2017; Yi and Cyster, 2013). Similarly, CD4$^+$ T cells, which are predominantly activated by cDC2s (Baptista et al., 2019; Dudziak et al., 2007; Eickhoff et al., 2015; Vander Lugt et al., 2014), congregate near the latter cells in an Ebi2-dependent manner (Baptista et al., 2019; Li et al., 2016). Consistent with this hypothesis, loss of CD4$^+$ cDC2s in Ebi2-deficient mice could be rescued by LTβR agonism (Yi and Cyster, 2013), suggesting that Ebi2 expression on cDCs controls access to LTα$_1$β$_2$. Alternatively, CCL20–CCR6 interactions might be involved. Both ILC3s and cDC2s express CCR6, and LTα$_1$β$_2$ leads to the induction of CCL20 (Kucharzik et al., 2002; Rumbo et al., 2004).

In summary, we showed here that splenic cDC homeostasis depends on both LTα$_1$β$_2$-expressing ILC3s and B cells. Synergism governs the overall size of the splenic cDC compartment and redundantly determines the terminal differentiation of Sirpα$^+$CD4$^+$Esam$^+$ cDC2s. Given the strong bias exhibited by the different cDC subsets in the induction of distinct T cell responses (den Haan et al., 2000; Dudziak et al., 2007; Lehmann et al., 2017; Schnorrer et al., 2006; Vander Lugt et al., 2014), our observations regarding the ability to manipulate the splenic Sirpα$^+$CD4$^+$Esam$^+$ cDC2 compartment in adulthood have relevance for the design of therapeutic approaches that aim to target CD4$^+$ T cell activity.

Materials and methods

Mice

Specific pathogen–free (SPF) WT C57BL/6 mice were obtained from Janvier Laboratories. Germ-free WT mice were bred and maintained at the University of Ghent gnotobiotic facility. B6.129S2-*Ighm*^{tm1Cgn}/J (*uMT*$^{-/-}$), B6(Cg)-*Rag2*$^{tm1.1Cgn}$/J (*Rag2*$^{-/-}$),

B6.129P2-*Gt(ROSA)26Sor*$^{tm1(DTA)Lky}$/J (DTA), B6.129P2(Cg)-*Rorc*^{tm2Litt}/J (*Rorgt*^{GFP}), B6.129P2(C)-*Cd19*$^{tm1(cre)Cgn}$/J (*CD19*-Cre), and B6.FVB-Tg$^{(Rorc-Cre)1Litt}$/J (*Rorc*-Cre) mice were obtained from The Jackson Laboratory. B6.B10(Cg)-*Rag2*^{tm1Fwa}*IL2rg*^{tm1Wjl} (*Rag2*$^{-/-}$ x $\gamma c^{-/-}$) mice were purchased from Taconic Farms. B6(Cg)-*Ncr1*$^{tm1.1(iCre)Viv}$ (*NKp46*-Cre; Narni-Mancinelli et al., 2011) and B6(Cg)-*Ltb*^{tm1Avt} (*Ltb*^{flox}; Tumanov et al., 2002) mice were described previously. All animals were maintained in SPF conditions at accredited animal facilities either at the VIB-UGhent or at the University of Texas at San Antonio. Housing conditions entailed individually ventilated cages in a controlled day–night cycle and food and water ad libitum. Unless stated otherwise, animals were enrolled in experiments between 8 and 12 wk of age. Both genders were used with no gender-specific effects being noticed. Animals were randomized into the different experimental groups blindly. Experiments were approved by either the VIB-UGhent ethical review board or the University of Texas at San Antonio Institutional Animal Care and Use Committee in accordance with the specific local legislation.

In vivo treatments

Antibiotic treatment

Mice were treated with broad-spectrum antibiotics (1 mg/ml ampicillin, 1 mg/ml neomycin, 1 mg/ml gentamycin, 1 mg/ml metronidazole, and 0.5 mg/ml vancomycin) targeting Gram-negative and -positive bacteria and protozoans in the drinking water (sugar supplemented to increase palatability) for 14 d.

Antibody-mediated cell depletion

To deplete NK cells or ILCs, 300 µg of rat anti-mouse NK1.1 (clone PK136; Bioceros) or 300 µg of rat anti-mouse CD90 (clone YTS154; Bioceros) was administered, respectively. Littermate controls were treated with an isotype control antibody (rat IgG2a, clone RG7/1.30; BioXCell).

LT$\alpha_1\beta_2$ antagonism

To block LT$\alpha_1\beta_2$ activity in vivo, mice were treated with an LTβR-Fc decoy receptor (Browning et al., 1997). Mice were injected intraperitoneally with 100 µg of this fusion protein on days 0, 3, 7, and 10 and analyzed on day 12 or 13. Control mice received identical injections of PBS.

LT$\alpha_1\beta_2$ agonism

LTβR agonism was induced by intraperitoneal injection of 100 µg of an agonistic rat anti-mouse LTβR antibody (clone 4H8; Bioceros), on days 0, 3, 7, and 10. Mice were sacrificed on day 12 or 13. Control mice received 100 µg of an isotype control antibody (rat IgG2a, clone RG7/1.30; BioXCell).

Adoptive ILC transfer

ILC expansion

To expand ILCs in vivo, *Rag2*$^{-/-}$ mice were treated intraperitoneally with a mixture of 2.5 µg recombinant human IL-7 (StemCell Technologies) and 15 µg mouse anti-human IL-7 antibody (clone M25; BioXCell) in PBS every other day for 1 wk.

ILC isolation and transfer

On day 6 of rhIL-7:anti–IL-7 treatment, the spleen, mesenteric lymph nodes, and small intestine were processed into single-cell suspensions, which were stained for FACS sorting. ILCs were sorted as live CD45$^+$Lineage(CD3e, CD19, NK1.1)$^-$ Ly6G$^-$CD11c$^-$CD90^{hi}CD127$^+$ cells on a FACSAria II (BD Biosciences). Approximately 4 × 10^5 ILCs were adoptively transferred via intrasplenic injection. Briefly, acceptor mice were anesthetized with isoflurane, the flank skin and peritoneum above the spleen were opened, and 100 µl of ILCs in PBS was injected directly into the spleen with a 29-G needle. The peritoneum was closed with surgical thread and the skin stapled. Buprenorphine analgesia (0.1 mg/kg) was administered subcutaneously. Littermate control mice underwent the same surgical procedure but received only PBS. Acceptor mice were analyzed 14 d after adoptive transfer.

Flow cytometry

Single cell-suspensions

Spleens were enzymatically digested with collagenase IV (3 mg/ml; Worthington) and DNase1 (40 µg/ml; Sigma-Aldrich) for 30 min at 37°C. Digestion was stopped by adding ice-cold PBS, and cell suspensions were filtered through a 70-µm nylon mesh. Bone marrow single-cell suspensions were obtained by flushing femurs with PBS over 70-µm nylon mesh filters. Erythrocytes were lysed in a solution of ammonium chloride (10 mM $KHCO_3$, 155 mM NH_4Cl, and 0.1 mM EDTA). To obtain cell counts, samples were spiked with counting beads (123count eBeads; Thermo Fisher Scientific).

Staining, acquisition, and analysis

Single-cell suspensions were first incubated with fixable viability dyes (eFluor506 or eFluor780; eBioscience) to identify dead cells and with an FcγRII/III antibody (clone 2.4G2) to limit nonspecific antibody binding. After washing, cells were incubated with mixtures of fluorescently and/or biotin-labeled antibodies for 30 min at 4°C. The antibodies used are listed in Table S1. When biotin-labeled antibodies were used, a second surface-staining step with fluorescently labeled streptavidin was included. For intracellular staining of transcription factors, cells were fixed using the Foxp3 fixation/permeabilization kit (eBioscience) per the manufacturer's instructions after surface staining. Samples were acquired on an LSRFortesssa cytometer (BD Biosciences) and analyzed using FlowJo software (BD Biosciences).

Immunofluorescence and image analysis

Immunofluorescence staining

Spleens were fixed in 1% paraformaldehyde, dehydrated in 30% sucrose, and frozen in optimal cutting temperature medium. 10-µm sections were prepared and stained overnight at 4°C. Antibodies are listed in Table S2.

Image acquisition, processing, and histocytometry

Multicolor images were acquired on a Zeiss 880 tiling confocal microscope equipped with 25×/0.8 numerical aperture and 40×/1.4 numerical aperture immersion oil objectives. The resulting

images were corrected for fluorochrome spillover in ImageJ and imported into Imaris for cellular visualization and segmentation. cDCs were visualized by selecting voxels with CD11c signal—the Imaris's surface creation wizard provided automatic thresholds around positively stained cells expediting this operation—and masking all other parameters of interest within using channel arithmetic operations in the ImarisXT extension. DC surfaces were created on the resulting CD11c channel using Imaris's surface creation module, which employs a watershed algorithm to define individual cells. ILC1s surfaces were segmented on NK1.1 signal and filtered for the absence of nuclear Eomes. ILC2s and ILC3s were segmented directly on Gata3 and Rorgt signals, respectively.

Spatial analysis

Following cellular segmentation and subset identification, individual cell statistics were imported in the R statistical environment for analysis. Positional data and subset identity were treated as multitype point patterns in two-dimensional space within the Spatstat package (Baddeley and Turner, 2005). Nearest neighbor distances between ILCs and cDCs were calculated with the nncross function. The conditional probability of observing a given cDC type as a function of the distance to ILCs was calculated with the mark connect function (markconnect in Spatstat),

$$Pij(r) = \frac{\lambda i \lambda j \; gij(r)}{\lambda_{\cdot}^{2} \; g(r)},$$

where λi, λj, and λ. are the intensities of cell types i, j, and of the two together, respectively; gij(r) is the cross-pair correlation function between types i and j; and g(r) is the pair correlation of the unmarked point process. For generation of null hypotheses (H_0) about the spatial distribution of cDCs and ILCs, two complementary approaches were used: (1) a fixed number of cDCs corresponding to the lowest number of cells from all subsets present in a given point pattern was randomly selected; and (2) the ILC marks were permutated at random across fixed positions using the rlabel function. For both approaches, 39 simulations were performed, yielding 95% confidence intervals.

Computational analysis of RNA sequencing data

Publicly available transcriptomic data regarding splenic cDCs and intestinal ILC3s were retrieved from GEO under accession no. GSE130201 (Brown et al., 2019) and accession no. GSE109125 (Immunological Genome Project Consortium), respectively. Here, we reanalyzed only bulk RNA sequencing profiles using the published count matrixes using R/Bioconductor.

Differential gene expression

To identify genes specifically associated with Tbet$^+$ (Sirpα$^+$CD4$^+$Esam$^+$) cDC2s, data were processed with edgeR (Robinson et al., 2010) for normalization and limma-voom (Ritchie et al., 2015) for pairwise differential expression testing. Genes were considered differentially expressed if $\log_2$ fold change > 1 or less than −1 (adjusted P value < 0.05, Benjamini–Hochberg correction for multiple testing). Of note, one Tbet$^-$ (Sirpα$^+$CD4$^-$Esam$^-$) cDC2 sample was removed from the analysis due to aberrant clustering as also seen in the original publication (Brown et al., 2019). For visualization, we used the package Triwise (van de Laar et al., 2016) reducing the three-dimensional dataset into a two-dimensional barycentric coordinate system displaying the $\log_2$ mean gene expression values of each cell type.

Gene ontology (GO) analysis

To obtain higher-order insights into the potential physiology of the Tbet$^+$ (Sirpα$^+$CD4$^+$Esam$^+$) cDC2 gene signature, we used clusterProfiler (Yu et al., 2012) to identify overrepresented GO terms. GO term redundancy was eliminated by calculating the semantic similarity between GO terms (Yu et al., 2010).

NicheNet analysis

To infer how ILC3s communicate with Tbet$^+$ (Sirpα$^+$CD4$^+$Esam$^+$) cDC2s, we used NicheNet (Browaeys et al., 2020). We assumed that the Tbet$^+$ cDC2 gene signature identified during differential gene expression testing partly represented the influence of ILC3s on Tbet$^+$ cDC2 gene expression; and we defined the sets of ligands and receptors expressed by ILC3s and Tbet$^+$ cDC2s, respectively, using edgeR. Subsequently, these data were used in NicheNet, using default parameters, to prioritize the ILC3-expressed ligands that explain the target gene signature. Potential Tbet$^+$ cDC2 receptors were identified by querying the NicheNet's built-in ligand-receptors prior models considering only bona fide interactions. To select hits for experimental validation, we further considered the absolute mRNA levels detected for each of the ligand-receptor pairs identified—$\log_2$(cpm).

Statistical analysis

Statistical analyses were performed with GraphPad Prism (GraphPad Software). The statistical methods used in each analysis are mentioned in the corresponding figure legends. Data are presented as bars representing the mean ± standard deviation; dots represent individual measurements. n.s., not significant; *, P < 0.05; **, P < 0.01; ***, P < 0.001; and ****, P < 0.0001.

Online supplemental material

Fig. S1 depicts the role of B cells, NK cells, and ILCs in splenic cDC homeostasis; Fig. S2 highlights the spatial localization of ILC and cDC subsets; and Fig. S3 shows the dependency of cDCs on $LT\alpha_1\beta_2$ signaling. Table S1 and Table S2 contain information regarding the antibodies used in this study.

Acknowledgments

We thank all members of the Laboratory of Immunoregulation and Mucosal Immunology (VIB-UGhent Center for Inflammation Research) for intellectual input during the course of these studies and the VIB Center for Inflammation Research Flow Cytometry and Microscopy Core Facilities for continuous assistance.

M. Vanderkerken is supported by a fellowship from Fonds Wetenschappelijk Onderzoek Vlaanderen; A.P. Baptista is

supported by a Marie-Sklodowska Curie Action fellowship as part of Horizon 2020; C.L. Scott is supported by the Fonds Wetenschappelijk Onderzoek Vlaanderen and a European Research Council starting grant; Y. Saeys is supported by the Fonds Wetenschappelijk Onderzoek Vlaanderen and the Marylou Ingram Scholar program; H. Hammad is supported by a research initiative grant from Ghent University; A.V. Tumanov is supported by grants from the National Institutes of Health (AI135574) and the Max and Minnie Tomerlin Voelcker Fund; and B.N. Lambrecht is supported by a European Research Council advanced grant, a research initiative grant from Ghent University, and an Excellence of Science research grant.

Author contributions: M. Vanderkerken designed, performed, and analyzed experiments and wrote the paper; A.P. Baptista conceptualized the research, designed, performed, and analyzed experiments, and wrote the paper; M. De Giovanni designed, performed, and analyzed experiments; S. Fukuyama, R. Browaeys, and C.L. Scott performed experiments; P.S. Norris, G. Eberl, J.P. Di Santo, E. Vivier, and Y. Saeys provided key reagents/materials; H. Hammad and J.G. Cyster designed and analyzed experiments; C.F. Ware and A.V. Tumanov designed experiments and provided key reagents; and C. De Trez and B.N. Lambrecht conceptualized the research, designed experiments, analyzed the data, and wrote the paper. All authors reviewed the paper.

Disclosures: E. Vivier is an employee of Innate Pharma. C.F. Ware reported grants from Capella Biosciences, grants from Eli Lilly, and grants from Boehringer Ingelheim Pharmaceuticals outside the submitted work; in addition, C.F. Ware had a patent to USP 8,974,787 issued and a patent to USP 8,349,320 issued. No other disclosures were reported.

Submitted: 9 May 2019
Revised: 12 September 2020
Accepted: 5 February 2021

References

Abe, K., F.O. Yarovinsky, T. Murakami, A.N. Shakhov, A.V. Tumanov, D. Ito, L.N. Drutskaya, K. Pfeffer, D.V. Kuprash, K.L. Komschlies, and S.A. Nedospasov. 2003. Distinct contributions of TNF and LT cytokines to the development of dendritic cells in vitro and their recruitment in vivo. *Blood.* 101:1477–1483. https://doi.org/10.1182/blood.V101.4.1477

Baddeley, A., and R. Turner. 2005. spatstat: An R package for analyzing spatial point patterns. *J. Stat. Softw.* 12:1–42. https://doi.org/10.18637/jss.v012.i06

Baptista, A.P., A. Gola, Y. Huang, P. Milanez-Almeida, P. Torabi-Parizi, J.F. Urban Jr., V.S. Shapiro, M.Y. Gerner, and R.N. Germain. 2019. The Chemoattractant Receptor Ebi2 Drives Intranodal Naive CD4$^+$ T Cell Peripheralization to Promote Effective Adaptive Immunity. *Immunity.* 50:1188–1201.e6. https://doi.org/10.1016/j.immuni.2019.04.001

Björklund, A.K., M. Forkel, S. Picelli, V. Konya, J. Theorell, D. Friberg, R. Sandberg, and J. Mjösberg. 2016. The heterogeneity of human CD127(+) innate lymphoid cells revealed by single-cell RNA sequencing. *Nat. Immunol.* 17:451–460. https://doi.org/10.1038/ni.3368

Bosteels, C., K. Neyt, M. Vanheerswynghels, M.J. van Helden, D. Sichien, N. Debeuf, S. De Prijck, V. Bosteels, N. Vandamme, L. Martens, et al. 2020. Inflammatory Type 2 cDCs Acquire Features of cDC1s and Macrophages to Orchestrate Immunity to Respiratory Virus Infection. *Immunity.* 52:1039–1056.e9. https://doi.org/10.1016/j.immuni.2020.04.005

Briseño, C.G., A.T. Satpathy, J.T. Davidson IV, S.T. Ferris, V. Durai, P. Bagadia, K.W. O'Connor, D.J. Theisen, T.L. Murphy, and K.M. Murphy. 2018. Notch2-dependent DC2s mediate splenic germinal center responses. *Proc. Natl. Acad. Sci. USA.* 115:10726–10731. https://doi.org/10.1073/pnas.1809925115

Browaeys, R., W. Saelens, and Y. Saeys. 2020. NicheNet: modeling intercellular communication by linking ligands to target genes. *Nat. Methods.* 17:159–162. https://doi.org/10.1038/s41592-019-0667-5

Brown, C.C., H. Gudjonson, Y. Pritykin, D. Deep, V.P. Lavallée, A. Mendoza, R. Fromme, L. Mazutis, C. Ariyan, C. Leslie, et al. 2019. Transcriptional Basis of Mouse and Human Dendritic Cell Heterogeneity. *Cell.* 179:846–863.e24. https://doi.org/10.1016/j.cell.2019.09.035

Browning, J.L., I.D. Sizing, P. Lawton, P.R. Bourdon, P.D. Rennert, G.R. Majeau, C.M. Ambrose, C. Hession, K. Miatkowski, D.A. Griffiths, et al. 1997. Characterization of lymphotoxin-alpha beta complexes on the surface of mouse lymphocytes. *J. Immunol.* 159:3288–3298.

Cabeza-Cabrerizo, M., J. van Blijswijk, S. Wienert, D. Heim, R.P. Jenkins, P. Chakravarty, N. Rogers, B. Frederico, S. Acton, E. Beerling, et al. 2019. Tissue clonality of dendritic cell subsets and emergency DCpoiesis revealed by multicolor fate mapping of DC progenitors. *Sci. Immunol.* 4:eaaw1941. https://doi.org/10.1126/sciimmunol.aaw1941

Calabro, S., D. Liu, A. Gallman, M.S. Nascimento, Z. Yu, T.T. Zhang, P. Chen, B. Zhang, L. Xu, U. Gowthaman, et al. 2016. Differential Intrasplenic Migration of Dendritic Cell Subsets Tailors Adaptive Immunity. *Cell Rep.* 16:2472–2485. https://doi.org/10.1016/j.celrep.2016.07.076

Cella, M., A. Fuchs, W. Vermi, F. Facchetti, K. Otero, J.K. Lennerz, J.M. Doherty, J.C. Mills, and M. Colonna. 2009. A human natural killer cell subset provides an innate source of IL-22 for mucosal immunity. *Nature.* 457:722–725. https://doi.org/10.1038/nature07537

Chu, C., S. Moriyama, Z. Li, L. Zhou, A.L. Flamar, C.S.N. Klose, J.B. Moeller, G.G. Putzel, D.R. Withers, G.F. Sonnenberg, and D. Artis. 2018. Antimicrobial Functions of Group 3 Innate Lymphoid Cells in Gut-Associated Lymphoid Tissues Are Regulated by G-Protein-Coupled Receptor 183. *Cell Rep.* 23:3750–3758. https://doi.org/10.1016/j.celrep.2018.05.099

Crowley, M.T., C.R. Reilly, and D. Lo. 1999. Influence of lymphocytes on the presence and organization of dendritic cell subsets in the spleen. *J. Immunol.* 163:4894–4900.

De Trez, C., K. Schneider, K. Potter, N. Droin, J. Fulton, P.S. Norris, S.W. Ha, Y.X. Fu, T. Murphy, K.M. Murphy, et al. 2008. The inhibitory HVEM-BTLA pathway counter regulates lymphotoxin receptor signaling to achieve homeostasis of dendritic cells. *J. Immunol.* 180:238–248. https://doi.org/10.4049/jimmunol.180.1.238

den Haan, J.M., S.M. Lehar, and M.J. Bevan. 2000. CD8(+) but not CD8(-) dendritic cells cross-prime cytotoxic T cells in vivo. *J. Exp. Med.* 192:1685–1696. https://doi.org/10.1084/jem.192.12.1685

Dudziak, D., A.O. Kamphorst, G.F. Heidkamp, V.R. Buchholz, C. Trumpfheller, S. Yamazaki, C. Cheong, K. Liu, H.W. Lee, C.G. Park, et al. 2007. Differential antigen processing by dendritic cell subsets in vivo. *Science.* 315:107–111. https://doi.org/10.1126/science.1136080

Eberl, G., S. Marmon, M.J. Sunshine, P.D. Rennert, Y. Choi, and D.R. Littman. 2004. An essential function for the nuclear receptor RORgamma(t) in the generation of fetal lymphoid tissue inducer cells. *Nat. Immunol.* 5:64–73. https://doi.org/10.1038/ni1022

Eickhoff, S., A. Brewitz, M.Y. Gerner, F. Klauschen, K. Komander, H. Hemmi, N. Garbi, T. Kaisho, R.N. Germain, and W. Kastenmüller. 2015. Robust Anti-viral Immunity Requires Multiple Distinct T Cell-Dendritic Cell Interactions. *Cell.* 162:1322–1337. https://doi.org/10.1016/j.cell.2015.08.004

Emgård, J., H. Kammoun, B. García-Cassani, J. Chesné, S.M. Parigi, J.M. Jacob, H.W. Cheng, E. Evren, S. Das, P. Czarnewski, et al. 2018. Oxysterol Sensing through the Receptor GPR183 Promotes the Lymphoid-Tissue-Inducing Function of Innate Lymphoid Cells and Colonic Inflammation. *Immunity.* 48:120–132.e8. https://doi.org/10.1016/j.immuni.2017.11.020

Fasnacht, N., H.Y. Huang, U. Koch, S. Favre, F. Auderset, Q. Chai, L. Onder, S. Kallert, D.D. Pinschewer, H.R. MacDonald, et al. 2014. Specific fibroblastic niches in secondary lymphoid organs orchestrate distinct Notch-regulated immune responses. *J. Exp. Med.* 211:2265–2279. https://doi.org/10.1084/jem.20132528

Fu, Y.X., G. Huang, Y. Wang, and D.D. Chaplin. 1998. B lymphocytes induce the formation of follicular dendritic cell clusters in a lymphotoxin alpha-dependent fashion. *J. Exp. Med.* 187:1009–1018. https://doi.org/10.1084/jem.187.7.1009

Gatto, D., K. Wood, I. Caminschi, D. Murphy-Durland, P. Schofield, D. Christ, G. Karupiah, and R. Brink. 2013. The chemotactic receptor EBI2 regulates the homeostasis, localization and immunological function of splenic dendritic cells. *Nat. Immunol.* 14:446–453. https://doi.org/10.1038/ni.2555

Gensollen, T., S.S. Iyer, D.L. Kasper, and R.S. Blumberg. 2016. How colonization by microbiota in early life shapes the immune system. *Science*. 352:539–544. https://doi.org/10.1126/science.aad9378

Gerner, M.Y., W. Kastenmuller, I. Ifrim, J. Kabat, and R.N. Germain. 2012. Histo-cytometry: a method for highly multiplex quantitative tissue imaging analysis applied to dendritic cell subset microanatomy in lymph nodes. *Immunity*. 37:364–376. https://doi.org/10.1016/j.immuni.2012.07.011

Gonzalez, M., F. Mackay, J.L. Browning, M.H. Kosco-Vilbois, and R.J. Noelle. 1998. The sequential role of lymphotoxin and B cells in the development of splenic follicles. *J. Exp. Med.* 187:997–1007. https://doi.org/10.1084/jem.187.7.997

Grajales-Reyes, G.E., A. Iwata, J. Albring, X. Wu, R. Tussiwand, W. Kc, N.M. Kretzer, C.G. Briseño, V. Durai, P. Bagadia, et al. 2015. Batf3 maintains autoactivation of Irf8 for commitment of a CD8α(+) conventional DC clonogenic progenitor. *Nat. Immunol.* 16:708–717. https://doi.org/10.1038/ni.3197

Gury-BenAri, M., C.A. Thaiss, N. Serafini, D.R. Winter, A. Giladi, D. Lara-Astiaso, M. Levy, T.M. Salame, A. Weiner, E. David, et al. 2016. The Spectrum and Regulatory Landscape of Intestinal Innate Lymphoid Cells Are Shaped by the Microbiome. *Cell*. 166:1231–1246.e13. https://doi.org/10.1016/j.cell.2016.07.043

Hoorweg, K., P. Narang, Z. Li, A. Thuery, N. Papazian, D.R. Withers, M.C. Coles, and T. Cupedo. 2015. A Stromal Cell Niche for Human and Mouse Type 3 Innate Lymphoid Cells. *J. Immunol.* 195:4257–4263. https://doi.org/10.4049/jimmunol.1402584

Kabashima, K., T.A. Banks, K.M. Ansel, T.T. Lu, C.F. Ware, and J.G. Cyster. 2005. Intrinsic lymphotoxin-beta receptor requirement for homeostasis of lymphoid tissue dendritic cells. *Immunity*. 22:439–450. https://doi.org/10.1016/j.immuni.2005.02.007

Kim, M.Y., F.M. McConnell, F.M. Gaspal, A. White, S.H. Glanville, V. Bekiaris, L.S. Walker, J. Caamano, E. Jenkinson, G. Anderson, and P.J. Lane. 2007. Function of CD4+CD3- cells in relation to B- and T-zone stroma in spleen. *Blood*. 109:1602–1610. https://doi.org/10.1182/blood-2006-04-018465

Kinnebrew, M.A., C.G. Buffie, G.E. Diehl, L.A. Zenewicz, I. Leiner, T.M. Hohl, R.A. Flavell, D.R. Littman, and E.G. Pamer. 2012. Interleukin 23 production by intestinal CD103(+)CD11b(+) dendritic cells in response to bacterial flagellin enhances mucosal innate immune defense. *Immunity*. 36:276–287. https://doi.org/10.1016/j.immuni.2011.12.011

Klose, C.S.N., M. Flach, L. Möhle, L. Rogell, T. Hoyler, K. Ebert, C. Fabiunke, D. Pfeifer, V. Sexl, D. Fonseca-Pereira, et al. 2014. Differentiation of type 1 ILCs from a common progenitor to all helper-like innate lymphoid cell lineages. *Cell*. 157:340–356. https://doi.org/10.1016/j.cell.2014.03.030

Kruglov, A.A., S.I. Grivennikov, D.V. Kuprash, C. Winsauer, S. Prepens, G.M. Seleznik, G. Eberl, D.R. Littman, M. Heikenwalder, A.V. Tumanov, and S.A. Nedospasov. 2013. Nonredundant function of soluble LTα3 produced by innate lymphoid cells in intestinal homeostasis. *Science*. 342:1243–1246. https://doi.org/10.1126/science.1243364

Kucharzik, T., J.T. Hudson III, R.L. Waikel, W.D. Martin, and I.R. Williams. 2002. CCR6 expression distinguishes mouse myeloid and lymphoid dendritic cell subsets: demonstration using a CCR6 EGFP knock-in mouse. *Eur. J. Immunol.* 32:104–112. https://doi.org/10.1002/1521-4141(200201)32:1<104::AID-IMMU104>3.0.CO;2-C

Lehmann, C.H.K., A. Baranska, G.F. Heidkamp, L. Heger, K. Neubert, J.J. Lühr, A. Hoffmann, K.C. Reimer, C. Brückner, S. Beck, et al. 2017. DC subset-specific induction of T cell responses upon antigen uptake via Fcγ receptors in vivo. *J. Exp. Med.* 214:1509–1528. https://doi.org/10.1084/jem.20160951

Lewis, K.L., M.L. Caton, M. Bogunovic, M. Greter, L.T. Grajkowska, D. Ng, A. Klinakis, I.F. Charo, S. Jung, J.L. Gommerman, et al. 2011. Notch2 receptor signaling controls functional differentiation of dendritic cells in the spleen and intestine. *Immunity*. 35:780–791. https://doi.org/10.1016/j.immuni.2011.08.013

Li, J., E. Lu, T. Yi, and J.G. Cyster. 2016. EBI2 augments Tfh cell fate by promoting interaction with IL-2-quenching dendritic cells. *Nature*. 533:110–114. https://doi.org/10.1038/nature17947

Liu, K., G.D. Victora, T.A. Schwickert, P. Guermonprez, M.M. Meredith, K. Yao, F.F. Chu, G.J. Randolph, A.Y. Rudensky, and M. Nussenzweig. 2009. In vivo analysis of dendritic cell development and homeostasis. *Science*. 324:392–397. https://doi.org/10.1126/science.1170540

Lu, E., E.V. Dang, J.G. McDonald, and J.G. Cyster. 2017. Distinct oxysterol requirements for positioning naïve and activated dendritic cells in the spleen. *Sci. Immunol.* 2:eaal5237. https://doi.org/10.1126/sciimmunol.aal5237

Ma, W., J. Lee, D. Backenroth, Y.J. Zhou, E. Bush, P. Sims, K. Liu, and Y. Shen. 2019. Single cell RNA-Seq reveals pre-cDCs fate determined by transcription factor combinatorial dose. *BMC Mol. Cell Biol.* 20:20. https://doi.org/10.1186/s12860-019-0199-y

Magri, G., M. Miyajima, S. Bascones, A. Mortha, I. Puga, L. Cassis, C.M. Barra, L. Comerma, A. Chudnovskiy, M. Gentile, et al. 2014. Innate lymphoid cells integrate stromal and immunological signals to enhance antibody production by splenic marginal zone B cells. *Nat. Immunol.* 15:354–364. https://doi.org/10.1038/ni.2830

Moseman, E.A., M. Iannacone, L. Bosurgi, E. Tonti, N. Chevrier, A. Tumanov, Y.X. Fu, N. Hacohen, and U.H. von Andrian. 2012. B cell maintenance of subcapsular sinus macrophages protects against a fatal viral infection independent of adaptive immunity. *Immunity*. 36:415–426. https://doi.org/10.1016/j.immuni.2012.01.013

Murphy, T.L., G.E. Grajales-Reyes, X. Wu, R. Tussiwand, C.G. Briseño, A. Iwata, N.M. Kretzer, V. Durai, and K.M. Murphy. 2016. Transcriptional Control of Dendritic Cell Development. *Annu. Rev. Immunol.* 34:93–119. https://doi.org/10.1146/annurev-immunol-032713-120204

Naik, S.H., P. Sathe, H.Y. Park, D. Metcalf, A.I. Proietto, A. Dakic, S. Carotta, M. O'Keeffe, M. Bahlo, A. Papenfuss, et al. 2007. Development of plasmacytoid and conventional dendritic cell subtypes from single precursor cells derived in vitro and in vivo. *Nat. Immunol.* 8:1217–1226. https://doi.org/10.1038/ni1522

Narni-Mancinelli, E., J. Chaix, A. Fenis, Y.M. Kerdiles, N. Yessaad, A. Reynders, C. Gregoire, H. Luche, S. Ugolini, E. Tomasello, et al. 2011. Fate mapping analysis of lymphoid cells expressing the NKp46 cell surface receptor. *Proc. Natl. Acad. Sci. USA*. 108:18324–18329. https://doi.org/10.1073/pnas.1112064108

Ngo, V.N., R.J. Cornall, and J.G. Cyster. 2001. Splenic T zone development is B cell dependent. *J. Exp. Med.* 194:1649–1660. https://doi.org/10.1084/jem.194.11.1649

Phan, T.G., J.A. Green, E.E. Gray, Y. Xu, and J.G. Cyster. 2009. Immune complex relay by subcapsular sinus macrophages and noncognate B cells drives antibody affinity maturation. *Nat. Immunol.* 10:786–793. https://doi.org/10.1038/ni.1745

Reboldi, A., T.I. Arnon, L.B. Rodda, A. Atakilit, D. Sheppard, and J.G. Cyster. 2016. IgA production requires B cell interaction with subepithelial dendritic cells in Peyer's patches. *Science*. 352:aaf4822. https://doi.org/10.1126/science.aaf4822

Ritchie, M.E., B. Phipson, D. Wu, Y. Hu, C.W. Law, W. Shi, and G.K. Smyth. 2015. limma powers differential expression analyses for RNA-sequencing and microarray studies. *Nucleic Acids Res.* 43:e47. https://doi.org/10.1093/nar/gkv007

Robinson, M.D., D.J. McCarthy, and G.K. Smyth. 2010. edgeR: a Bioconductor package for differential expression analysis of digital gene expression data. *Bioinformatics*. 26:139–140. https://doi.org/10.1093/bioinformatics/btp616

Rumbo, M., F. Sierro, N. Debard, J.P. Kraehenbuhl, and D. Finke. 2004. Lymphotoxin beta receptor signaling induces the chemokine CCL20 in intestinal epithelium. *Gastroenterology*. 127:213–223. https://doi.org/10.1053/j.gastro.2004.04.018

Sathe, P., and K. Shortman. 2008. The steady-state development of splenic dendritic cells. *Mucosal Immunol.* 1:425–431. https://doi.org/10.1038/mi.2008.56

Satpathy, A.T., C.G. Briseño, J.S. Lee, D. Ng, N.A. Manieri, W. Kc, X. Wu, S.R. Thomas, W.L. Lee, M. Turkoz, et al. 2013. Notch2-dependent classical dendritic cells orchestrate intestinal immunity to attaching-and-effacing bacterial pathogens. *Nat. Immunol.* 14:937–948. https://doi.org/10.1038/ni.2679

Schaeuble, K., M.R. Britschgi, L. Scarpellino, S. Favre, Y. Xu, E. Koroleva, T.K.A. Lissandrin, A. Link, M. Matloubian, C.F. Ware, et al. 2017. Perivascular Fibroblasts of the Developing Spleen Act as LTα1β2-Dependent Precursors of Both T and B Zone Organizer Cells. *Cell Rep.* 21:2500–2514. https://doi.org/10.1016/j.celrep.2017.10.119

Schlitzer, A., V. Sivakamasundari, J. Chen, H.R. Sumatoh, J. Schreuder, J. Lum, B. Malleret, S. Zhang, A. Larbi, F. Zolezzi, et al. 2015. Identification of cDC1- and cDC2-committed DC progenitors reveals early lineage priming at the common DC progenitor stage in the bone marrow. *Nat. Immunol.* 16:718–728. https://doi.org/10.1038/ni.3200

Schnorrer, P., G.M. Behrens, N.S. Wilson, J.L. Pooley, C.M. Smith, D. El-Sukkari, G. Davey, F. Kupresanin, M. Li, E. Maraskovsky, et al. 2006. The dominant role of CD8+ dendritic cells in cross-presentation is not dictated by antigen capture. *Proc. Natl. Acad. Sci. USA*. 103:10729–10734. https://doi.org/10.1073/pnas.0601956103

Sichien, D., B.N. Lambrecht, M. Guilliams, and C.L. Scott. 2017. Development of conventional dendritic cells: from common bone marrow progenitors

to multiple subsets in peripheral tissues. *Mucosal Immunol.* 10:831–844. https://doi.org/10.1038/mi.2017.8

Tumanov, A., D. Kuprash, M. Lagarkova, S. Grivennikov, K. Abe, A. Shakhov, L. Drutskaya, C. Stewart, A. Chervonsky, and S. Nedospasov. 2002. Distinct role of surface lymphotoxin expressed by B cells in the organization of secondary lymphoid tissues. *Immunity.* 17:239–250. https://doi.org/10.1016/S1074-7613(02)00397-7

Tussiwand, R., B. Everts, G.E. Grajales-Reyes, N.M. Kretzer, A. Iwata, J. Bagaitkar, X. Wu, R. Wong, D.A. Anderson, T.L. Murphy, et al. 2015. Klf4 expression in conventional dendritic cells is required for T helper 2 cell responses. *Immunity.* 42:916–928. https://doi.org/10.1016/j.immuni.2015.04.017

van de Laar, L., W. Saelens, S. De Prijck, L. Martens, C.L. Scott, G. Van Isterdael, E. Hoffmann, R. Beyaert, Y. Saeys, B.N. Lambrecht, and M. Guilliams. 2016. Yolk Sac Macrophages, Fetal Liver, and Adult Monocytes Can Colonize an Empty Niche and Develop into Functional Tissue-Resident Macrophages. *Immunity.* 44:755–768. https://doi.org/10.1016/j.immuni.2016.02.017

van de Pavert, S.A., and R.E. Mebius. 2010. New insights into the development of lymphoid tissues. *Nat. Rev. Immunol.* 10:664–674. https://doi.org/10.1038/nri2832

Vander Lugt, B., A.A. Khan, J.A. Hackney, S. Agrawal, J. Lesch, M. Zhou, W.P. Lee, S. Park, M. Xu, J. DeVoss, et al. 2014. Transcriptional programming of dendritic cells for enhanced MHC class II antigen presentation. *Nat. Immunol.* 15:161–167. https://doi.org/10.1038/ni.2795

Vivier, E., D. Artis, M. Colonna, A. Diefenbach, J.P. Di Santo, G. Eberl, S. Koyasu, R.M. Locksley, A.N.J. McKenzie, R.E. Mebius, et al. 2018. Innate Lymphoid Cells: 10 Years On. *Cell.* 174:1054–1066. https://doi.org/10.1016/j.cell.2018.07.017

Wang, Y.G., K.D. Kim, J. Wang, P. Yu, and Y.X. Fu. 2005. Stimulating lymphotoxin beta receptor on the dendritic cells is critical for their homeostasis and expansion. *J. Immunol.* 175:6997–7002. https://doi.org/10.4049/jimmunol.175.10.6997

Weizman, O.E., N.M. Adams, I.S. Schuster, C. Krishna, Y. Pritykin, C. Lau, M.A. Degli-Esposti, C.S. Leslie, J.C. Sun, and T.E. O'Sullivan. 2017. ILC1 Confer Early Host Protection at Initial Sites of Viral Infection. *Cell.* 171:795–808.e12. https://doi.org/10.1016/j.cell.2017.09.052

Wu, Q., Y. Wang, J. Wang, E.O. Hedgeman, J.L. Browning, and Y.X. Fu. 1999. The requirement of membrane lymphotoxin for the presence of dendritic cells in lymphoid tissues. *J. Exp. Med.* 190:629–638. https://doi.org/10.1084/jem.190.5.629

Yi, T., and J.G. Cyster. 2013. EBI2-mediated bridging channel positioning supports splenic dendritic cell homeostasis and particulate antigen capture. *eLife.* 2:e00757. https://doi.org/10.7554/eLife.00757

Yu, G., F. Li, Y. Qin, X. Bo, Y. Wu, and S. Wang. 2010. GOSemSim: an R package for measuring semantic similarity among GO terms and gene products. *Bioinformatics.* 26:976–978. https://doi.org/10.1093/bioinformatics/btq064

Yu, G., L.G. Wang, Y. Han, and Q.Y. He. 2012. clusterProfiler: an R package for comparing biological themes among gene clusters. *OMICS.* 16:284–287. https://doi.org/10.1089/omi.2011.0118

Zindl, C.L., T.H. Kim, M. Zeng, A.S. Archambault, M.H. Grayson, K. Choi, R.D. Schreiber, and D.D. Chaplin. 2009. The lymphotoxin LTalpha(1)beta(2) controls postnatal and adult spleen marginal sinus vascular structure and function. *Immunity.* 30:408–420. https://doi.org/10.1016/j.immuni.2009.01.010

Supplemental material

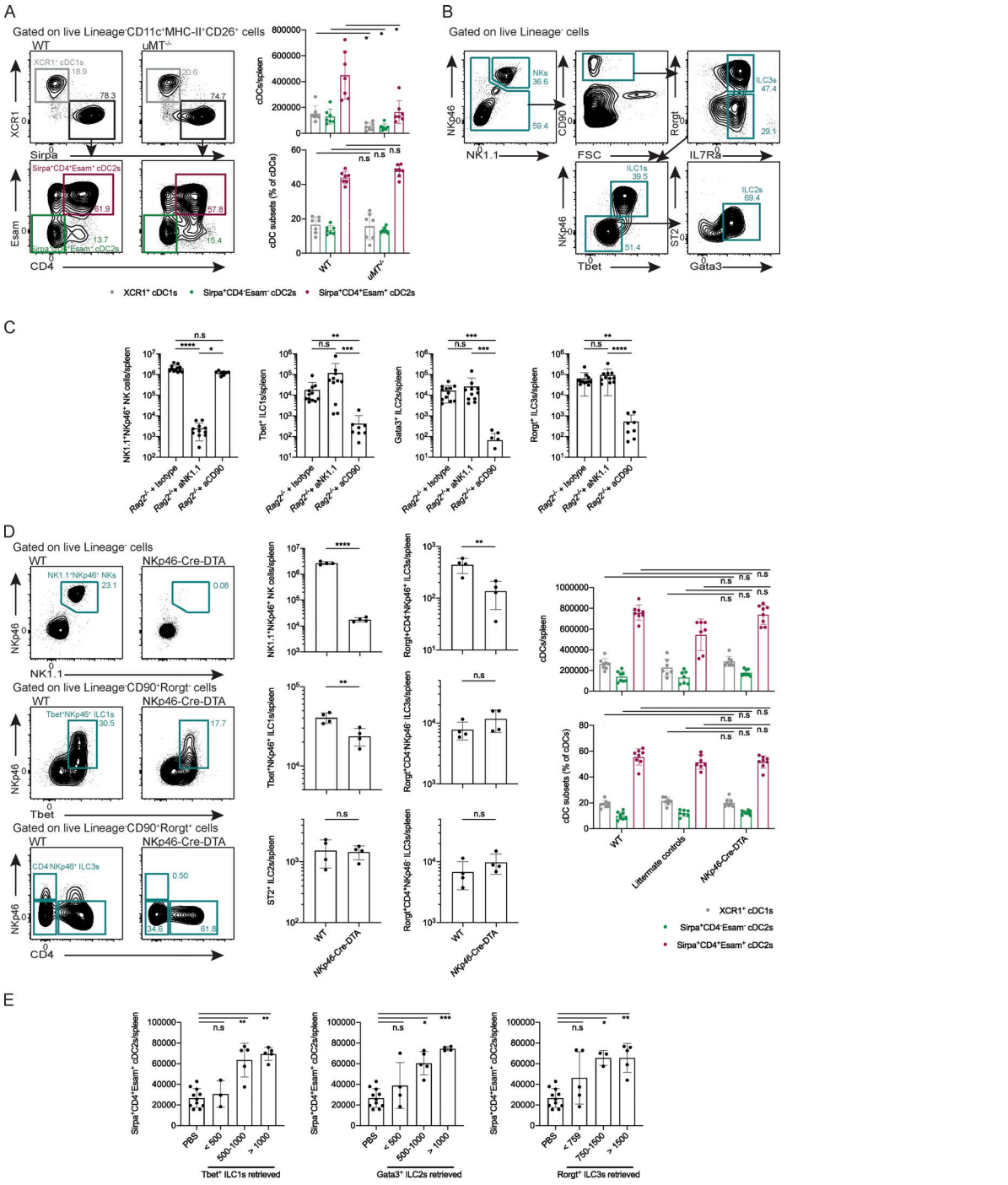

Figure S1. **B cells and NK cells are dispensable for the terminal differentiation of Sirpα⁺CD4⁺Esam⁺ cDC2s. (A)** Representative flow cytometry plots and quantification of cDCs in the spleens of WT and *uMT*$^{-/-}$ mice. *n* = 7 WT mice, and 7 uMT$^{-/-}$ mice; two independent experiments; two-way ANOVA with Sidak's multiple comparisons post-test. **(B)** Gating strategy for the identification and quantification of NK cells and ILCs. NK cells are defined as Lineage(CD3e/CD19/Ter119)$^{-}$NK1.1^{hi}NKp46^{hi} cells. ILCs are identified as Lineage(CD3e/CD19/Ter119)$^{-}$NK1.1$^{-/low}$NKp46$^{-/low}$CD90^{+} cells. The different ILC subsets are further defined based on the expression of IL7Ra, Rorgt, NKp46, Tbet, Gata3, and ST2. **(C)** Quantification of innate lymphocytes in the spleen of mice treated with depleting NK1.1 or CD90 antibodies. *n* = 12 *Rag2*$^{-/-}$ + isotype antibody control mice, 11 *Rag2*$^{-/-}$ + aNK1.1 mice, and 8 *Rag2*$^{-/-}$ + aCD90 mice; at least two independent experiments per treatment regimen; Kruskal–Wallis test with Dunn's multiple comparisons post-test. **(D)** Representative flow cytometry plots of selected innate lymphocyte populations and quantification of innate lymphocytes and cDC in the spleen of WT and NKp46-DTA mice. *n* = 4 WT mice, and 4 *NKp46-DTA* mice for ILC quantification; one experiment; Mann–Whitney *U* test. *n* = 8 WT mice, 7 littermate WT control mice, and 8 *NKp46-DTA* mice for cDC quantification; two independent experiments; two-way ANOVA with Sidak's multiple comparisons post-test. **(E)** Quantification of splenic Sirpa⁺CD4⁺Esam⁺ cDC2s in the spleens of Rag2$^{-/-}$ γc$^{-/-}$ mice following adoptive transfer of ILCs. *n* = 11 *Rag2*$^{-/-}$ x γc $^{-/-}$ PBS control mice, 13 *Rag2*$^{-/-}$ x γc$^{-/-}$ + ILCs; three independent experiments. Results are discretized by the recovery rates of Tbet⁺ ILC1s, Gata3⁺ ILC2s, and Rorgt⁺ ILC3s, with the number of samples in each group varying according to the number of ILCs of each type recovered. Kruskal–Wallis test with Dunn's multiple comparisons post-test. *, P < 0.05; **, P < 0.01; ***, P < 0.001; ****, P < 0.0001.

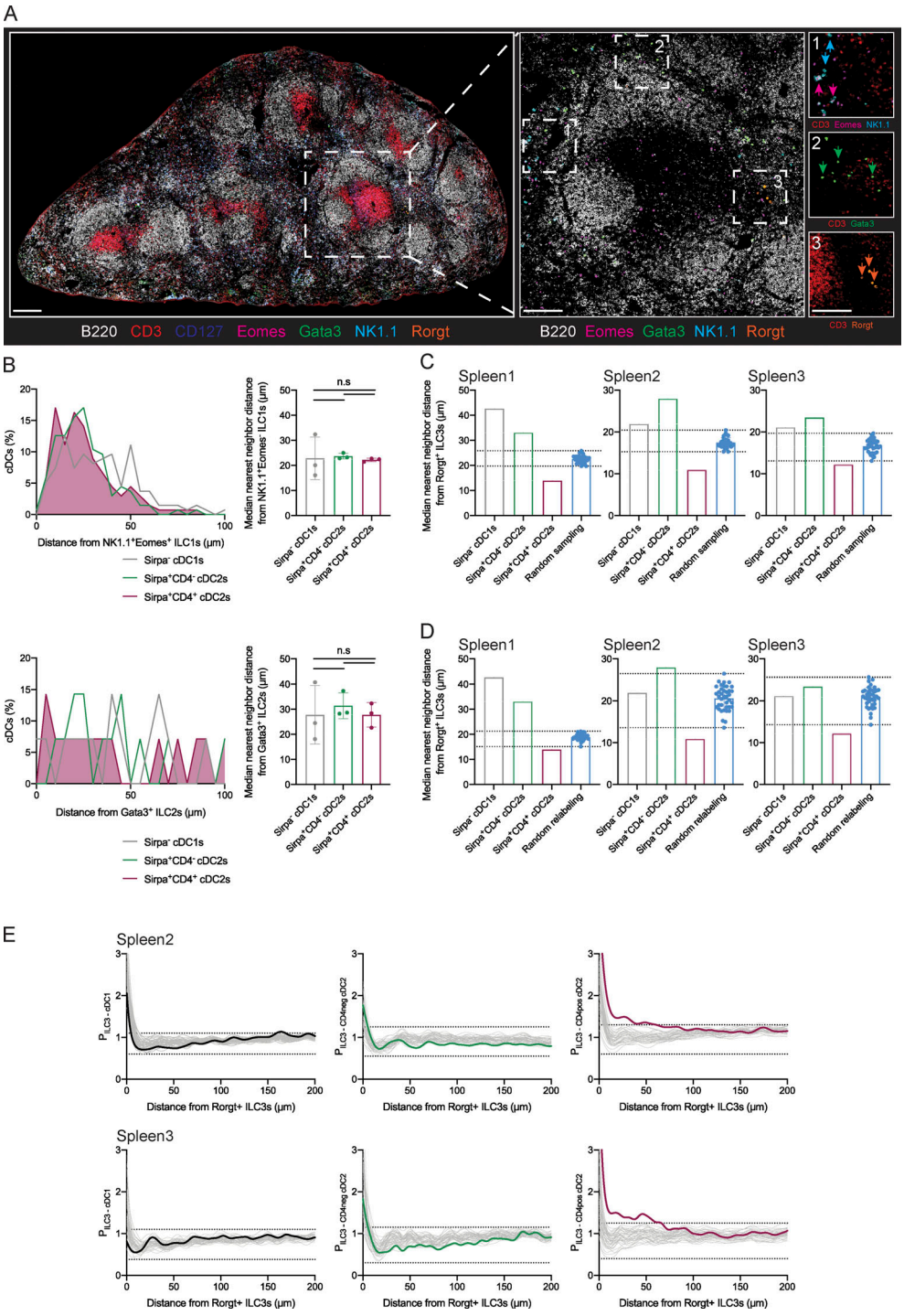

Figure S2. **Splenic ILCs are inhomogenously distributed. (A)** Representative immunofluorescence image of WT splenic ILCs. Spleen sections were stained with the indicated markers, allowing identification of the major anatomical regions and ILCs subsets. NK cells were identified as CD3⁻NK1.1⁺Eomes⁺ cells (purple arrows), ILC1s were identified as CD3⁻NK1.1⁺Eomes⁻ cells (cyan arrows), ILC2s were identified as CD3⁻Gata3⁺ cells (green arrows), and ILC3s were CD3⁻Rorgt⁺ (orange arrows). *n* = 3 spleens. Scale bars, 200 µm for low-magnification images, 100 µm for zoomed-in insets. **(B)** Spatial frequency distribution of WT cDCs around NK1.1⁺Eomes⁺ ILC1s and Gata3⁺ ILC2s for the example shown in Fig. 3 A and median nearest neighbor distance. *n* = 3 spleens. Repeated-measures ANOVA with Tukey's multiple comparisons post-test. **(C)** Median nearest neighbor distance of WT cDCs toward Rorgt⁺ ILC3s per spleen analyzed. Observed values for Sirpα⁻ cDC1s, Sirpα⁺CD4⁻ cDC2s, and Sirpα⁺CD4⁺ cDC2s are shown in gray, green, and purple, respectively. Distances between Rorgt⁺ ILC3s and randomly sampled Sirpα⁺CD4⁺ cDC2s are shown in cyan (*n* = 39); the boundaries of the simulated datasets are depicted by the dotted lines. **(D)** Median nearest neighbor distance of WT cDCs toward Rorgt⁺ ILC3s per spleen analyzed. Observed values for Sirpα⁻cDC1s, Sirpα⁺CD4⁻ cDC2s, and Sirpα⁺CD4⁺ cDC2s are shown in gray, green, and purple, respectively. Distances between randomly relabeled Rorgt⁺ ILC3s and Sirpα⁺CD4⁺ cDC2s are shown in cyan (*n* = 39); the boundaries of the simulated datasets are depicted by the dotted lines. **(E)** Probability of observing a cDC of a given subset as a function of spatial distance from Rorgt⁺ ILC3s in the two additional spleens analyzed. The observed probability is shown in bold. The result of randomly relabeling Rorgt⁺ ILC3s across the ILC repertoire is shown in gray (*n* = 39). The upper and lower boundary values for those simulations are depicted by the dotted lines.

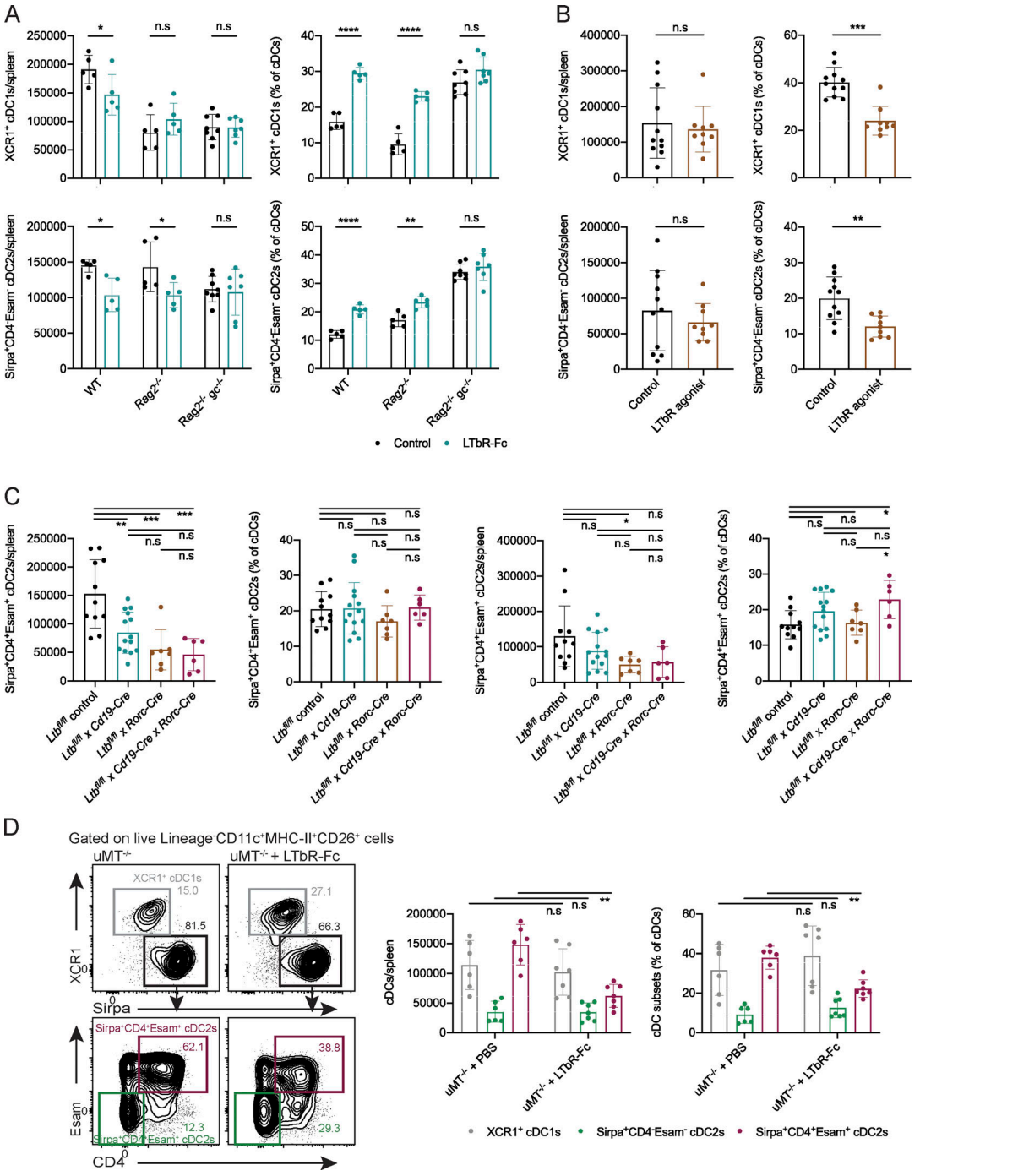

Figure S3. **XCR1⁺ cDC1s and Sirpα⁺CD4⁻Esam⁻ cDC2s are minimally affected by manipulation of the LTα$_1$β$_2$ pathway. (A)** Quantification of splenic XCR1⁺ cDC1s and Sirpα⁺CD4⁻Esam⁻ cDC2s in WT, *Rag2*$^{-/-}$, and *Rag2*$^{-/-}$ x *γc* $^{-/-}$ mice treated with the antagonist LTβR-Fc decoy receptor. *n* = 5 control + 5 LTβR-Fc-treated WT mice, 5 control + 5 LTβR-Fc-treated *Rag2*$^{-/-}$ mice, and 8 control + 7 LTβR-Fc-treated *Rag2*$^{-/-}$ x *γc*$^{-/-}$ mice; two independent experiments per genotype; two-way ANOVA with Sidak's multiple comparisons post-test. **(B)** Quantification of splenic XCR1⁺ cDC1s and Sirpα⁺CD4⁻Esam⁻ cDC2s in *Rag2*$^{-/-}$ x *γc* $^{-/-}$ mice treated with an agonist LTβR antibody. *n* = 11 *Rag2*$^{-/-}$ x *γc* $^{-/-}$ mice treated with control antibody, and 9 *Rag2*$^{-/-}$ x *γc*$^{-/-}$ mice treated with anti-LTβR; three independent experiments; Mann–Whitney *U* test. **(C)** Quantification of splenic XCR1⁺ cDC1s and Sirpα⁺CD4⁻Esam⁻ cDC2s in *Ltb*$^{flox/flox}$ control, *Ltb*$^{flox/flox}$ x *Cd19-Cre*, *Ltb*$^{flox/flox}$ x *Rorc-Cre*, and *Ltb*$^{flox/flox}$ x *Cd19-Cre* x *Rorc-Cre* mice. *n* = 11 *Ltb*$^{flox/flox}$ control, 15 *Ltb*$^{flox/flox}$ x *Cd19-Cre*, 7 *Ltb*$^{flox/flox}$ x *Rorc-Cre*, and 6 *Ltb*$^{flox/flox}$ x *Cd19-Cre* x *Rorc-Cre* mice; data verified in at least two independent experiments per genotype; Kruskal–Wallis test with Dunn's multiple comparisons post-test. **(D)** Representative flow cytometry plots and quantification of splenic cDCs in *uMT*$^{-/-}$ mice treated with the antagonist LTβR-Fc decoy receptor. *n* = 6 control + 7 LTβR-Fc–treated mice; two independent experiments; two-way ANOVA with Sidak's multiple comparisons post-test. *, P < 0.05; **, P < 0.01; ***, P < 0.001; ****, P < 0.0001.

Two tables are provided online. Table S1 lists the antibodies used for flow cytometry in this paper. Table S2 lists the antibodies used for immunofluorescence imaging in this paper.